8-2018

Complex Oxide Thin Films from Perovskite to Pyrochlore

Clayton Russell Frederick
University of Tennessee, cfreder3@vols.utk.edu

To the Graduate Council:

I am submitting herewith a thesis written by Clayton Russell Frederick entitled "Complex Oxide Thin Films from Perovskite to Pyrochlore." I have examined the final electronic copy of this thesis for form and content and recommend that it be accepted in partial fulfillment of the requirements for the degree of Master of Science, with a major in Physics.

Jian Liu, Major Professor

We have read this thesis and recommend its acceptance:

Norman Mannella, Haidong Zhou

Accepted for the Council:
Dixie L. Thompson

Vice Provost and Dean of the Graduate School

(Original signatures are on file with official student records.)

Complex Oxide Thin Films from Perovskite to Pyrochlore

A Thesis Presented for the

Master of Science

Degree

The University of Tennessee, Knoxville

Clayton Russell Frederick

August 2018

Abstract

The world of condensed matter physics is a fascinating field. With all of the many different elements to explore, it seems impossible to discover all of their secrets. Nevertheless, a study of two different materials is covered in this work. The first type of materials are the Perovskites; these materials are commonly used in materials research, but still have hidden treasures left for research scientist to explore. The second type of materials are the Pyrochlores. The Pyrochlores are not as widely studied as the Perovskite materials, thus, leaving even more avenues to venture down in the quest to learn the ways of nature and the properties of these materials. In this work, the valence electron states and the magnetic properties of the Perovskite LMO on STO are reported with the samples varying in thickness from 3 – unit cells to 12 – unit cells were measured and the results reported for their XAS measurements. In addition, the growth of the Pyrochlore YTO on YSZ are, also, investigated using XRD and differing growth conditions to ascertain the ideal growth conditions for the material. Furthermore, an overview of the experimental techniques is included to assist in understanding the results of this thesis. Finally, a summary of the results and an outlook for future work is included.

Table of Contents

List of Tables

List of Figures

List of Abbreviations and Symbols

AFM	Atomic Force Microscope
NGO	Neodymium Gallium Oxide ($NdGaO_3$)
PLD	Pulsed Laser Deposition
STO	Strontium Titanium Oxide ($SrTiO_3$)
XAS	X-Ray Absorption Spectroscopy
XRD	X-Ray Diffraction
YSZ	Yttrium Stabilized Zirconium
YTO	Yttrium Titanium Oxide ($Y_2Ti_2O_7$)
ZDSO	Zinc Dysprosium Antimony Oxide ($Zn_2Dy_3Sb_3O_{14}$)

Chapter 1: Introduction

Material Science is an extremely popular and exciting scientific field. This interest stems from the many different properties, which are controllable down to the atomic level, and can produce novel effects in a plethora of materials. Despite this controllability, there are still many aspects, which are not, yet, well understood, but are extremely necessary, and highly studied, for all of the fascinating results produced. Along these lines, Perovskite materials are commonly used for materials research. Additionally, Pyrochlore materials are of special interest, and are a playground for materials scientists as well. Furthermore, they have not been as widely studied as the Perovskite materials. Pyrochlore materials have the $A_2B_2O_7$ structure. These materials have many interesting properties including: ionic conductivity [1], optical nonlinearity [2], and high radiation tolerance [3]. Along with these properties, the pyrochlore materials, potentially, have numerous applications for example: thermal barrier coating [4], high-permittivity dielectrics [5], solid electrolytes in solid-oxide fuel cells [6], and materials for safely disposing of nuclear waste containing actinide [7]. Along these same lines, if the A site of the material is Y, or any other rare earth element for that matter, and the B site is Ti you will get the structure as in Figure 1.1 [8]. One of the most interesting phenomena demonstrated by these materials is frustration. Frustration has become a focus of these materials due to the work of J. Villian [9]. Frustration was first identified as crystalline ice with disorder and with the frustration continuing to an extremely low temperature [10]. The specific Pyrochlore material synthesized in this work is $Y_2Ti_2O_7$ (YTO) (Figure 1.1a). One of the reasons for this is because the Y is nonmagnetic making YTO an excellent buffer material placed on the Yttrium Stabilized Zirconium (YSZ) substrate which is not very conducive to growing some pyrochlore oxide films. Also, YTO has a better lattice match for the next phase of the overall project some of which will be discussed at a later section of this work. Growing YTO on YSZ along the [111] direction (Figure 1.1b) allows the tailoring of the frustration in the desired materials along a specific (desired) direction or plane. Motivation: Our final goal is to grow a $Zn_2Dy_3Sb_3O_{14}$ (ZDSO) frustrated magnet. To do this, we needed to lay a foundation for optimum growth. We started substrate treatment and moved on to growing a YTO film for a more conducive environment for ZDSO growth.

1.1 Overview of thesis

This work is an overview of important experimental methods and applications of materials research, as such, it is composed of five chapters all of which illustrate or explain one or more applications and/or methods. In this chapter, an overview of this work is described. Chapter 2 gives a brief overview of the experimental methods used. Chapter 3 is a $LaMnO_3$ (LMO)/$SrTiO_3$ (STO) project and illustrates the usage of experimental methods, some substrate treatment, and analysis of XAS data conducted by the author. Chapter 4 is another project dealing with the growth and characterization of YTO on YSZ substrates along with the treatment of the substrates. Furthermore, chapter 4 talks about the materials synthesized by the author concluding with the analysis of the samples; with chapter 5 looking to future work and research possibilities and providing a summary of the overall thesis.

Chapter 2: Experimental Methods

2.1 Pulsed Laser Deposition

There are many ways to create thin films, but the 3 principle methods for making them are: first, Molecular Beam Epitaxy, second, Pulsed Laser Deposition (PLD), and, lastly, the Sputtering Method. Pulsed Laser Deposition is a method used to make, typically called growth, thin films through the ablation (evaporation) of material with a laser. This technique produces high quality films in a relatively short time period and at cheaper costs than some other epitaxial methods. The earliest accounts of any type of laser ablation experiments was in the 1960s by Breech and Cross [22] at the International Conference on Spectroscopy. In this work, a ruby laser vaporized and excited atoms from solid surfaces with the photon spectrum being used to identify the elements of the ejecting surface. As with most scientific instruments, commercial ones appeared shortly afterwards.

In the first experimental paper, researchers Honig and Woolston [23] studied the laser ablation of multiple metals, semiconductors and of insulators. But, if we fast forward to the nineties, the assuredness of laser ablation and its applications would benefit scientific research and development. This fact was supported by the very first conference specifically for laser ablation hosted at Oak Ridge National Laboratory [24]. With the advent of high-temperature superconductors, the benefits of PLD were finally realized [25]. The appropriate growth conditions were achieved using PLD even with the complex composition of multi-elementary materials [26].

In PLD, you need a substrate, a target and holder, laser, heater. The substrate is mounted onto a plate which is attached to some type of heater, either laser or resistive, and placed inside a vacuum chamber. This can be either high vacuum or ultra-high vacuum. Inside the chamber, there is also the target and target holder. The target(s) is a compressed pellet made of the material that is to be grown inside the chamber. Typically, a UV laser is used to produce, or fire, a short and intense pulse (shot) striking the target for the growth process (See figure 2.1).

Since every material is different, there are a plethora of varying ideal conditions for each one of them, and it is difficult to have all of these conditions satisfied. Some of the constraints on the growth include: pressure inside the chamber, composition of the gas inside, temperature, spot size and shape of the laser, the composition and type of the target used, the laser fluency, and the density of the plasma plume. The PLD process allows for control and tunability of the material even down to the atomic layer.

Other than the aforementioned deposition conditions, there are a few other important parameters which affect the growth and separates PLD from the other techniques: 1. the high energy of the particles attaching to the substrate, 2. the deposition rates that are achieved, and 3. the pulsed deposition [27]. Starting with the plasma plume, its characteristics can be classified into charged and neutral. Out of these two, the charged has the highest kinetic energy (as much as 250eV). Despite the higher energy, there still exists a substantial interaction of the ablated material and ambient gas molecules [28]. The majority of this energy is diffused by the gas in the environment due to interactions with colder gas molecules. The nature of the growth is reliant on the velocity of the incoming ablated particles which is regulated by the pressure of the gas in the chamber (equation 11) and the distance between the target and the substrate.

1. $$\frac{j_{E,g}}{j_{E,v}} = \frac{n_g}{n_v}\left(\frac{v_g}{v_v}\right)^3$$

With j_E being the energy supply rate; n is the particle flux, v_g and v_v are the forward velocities of the particles in the gas; v_v is the forward velocity of the particles in vacuum; where the subscript g is the gas and v is vacuum. Due to the fact that the plasma plume is composed of many different types of materials, the theoretical explanations of the velocity distribution can be arduous. The models conclude that the velocity of the particles landing on the substrate is a function of the gas pressure; thus, a heavy influence from the gas pressure is normal [27]. Due to the stress from the high energy particles on grown films, the gas inside the chamber behaves as a buffer for the high velocity particles and slows their movement.

2.2 Atomic Force Microscopy

Atomic Force Microscopy (AFM) is a tool for characterization of thin films. AFM is widely used for developing, optimizing, and monitoring the deposition process and helps to understand relationships between the properties of the film. Some of the commonly measured properties include: surface roughness, uniformity, and morphology; mechanical properties, hardness, and wear; conductivity, permittivity, stored charge, and various other electrical properties; piezoelectric / electromechanical response; magnetic properties; thermal properties. AFM is extremely useful in imaging topography of nanoscale materials. It was discovered in 1980s by G. Binnig, C.F. Quate, and Ch. Gerber [11]. In their paper, they introduce a way for a scanning tunneling microscope to measure the motion of a cantilever with ultrasmall mass along with forces as small as 10^{-18}N and distances of 10^{-4} angstroms. The images are acquired by measuring the force on a sharp tip created by the proximity of the sample surface while keeping the force small and constant [11]. When the tip is moved sideways along the surface it can trace the contours of the material being measured. In the AFMs of today, typically, a laser is used to align the tip and in the most opportune position for imaging. During the imaging process, the tip is oscillated at resonance by a specific voltage and amplitude. This allows for the detection of changes in topography as the AFM adjusts the position of the tip to keep the cantilever oscillating at the appropriate voltage, frequency, and amplitude. The three dimensional images enable nanoscale information on the film

structure to be obtained. The AFM vibrates a cantilever at a specific frequency and voltage, thus, allowing it to map the surface of the material and detect any changes in the material's topography. The AFM is able to measure the extremely small force between the cantilever and the sample because the cantilever is approximately 3-6μm in height with a radius of 15-40nm. The AFM is strong at detecting the vertical changes in the topography of materials with a resolution up to 0.1nm. This is accomplished by measuring the vertical and even the lateral deflections of the cantilever by the use of an optical lever. The basic theory for this is Hooke's Law:

$$2. \quad F = -kx$$

Where F is the force, k is the spring constant, and x is the cantilever deflection. When the spring constant of the cantilever is less than that of the surface (~0.1-1 N/m), the cantilever will bend. As the cantilever bends the deflection is measured. The detected forces range from nN to μN in open air [12]. There are three primary modes of imaging in AFM (depending on make and model): first, Contact mode; Second, Tapping Mode; Third, Non-Contact Mode. In this work,only the tapping mode was utilized; therefore, a more in-depth explanation will be covered.

The Tapping mode is very similar to the contact mode, but, in tapping mode, the cantilever is oscillated at its resonant frequency. Since the spring is critical in AFM, and the maximum deflection for the given force is needed. The spring must be as soft as possible, but, also, needs to be stiff for it to have a high resonant frequency in order to help minimize the vibrational sensitivity. The resonant frequency is given in equation 2:

$$3. \quad f_0 = \left(\frac{1}{2\pi}\right)\left(\frac{k}{m_0}\right)^{\frac{1}{2}}$$

With f_0 is the resonant frequency; k is the spring constant; m_0 is the effective mass that loads the spring. With the above equation, it can be seen that the ration of k/m_0 must be kept large; therefore, when k is increased (or decreased), m_0 must also increase (or decrease) as well. With a known resonance frequency, the tip taps the sample's surface while scanning, thus, making contact with the sample at the bottom end of the oscillation. As mentioned above, the cantilever is driven at a specific amplitude and at the resonance frequency allowing the AFM to detect changes in the surface when an adjustment in the cantilever is necessary in order to keep the amplitude constant.

2.3 X-Ray Diffraction

Remembering that X-Rays are electromagnetic radiation with energies ranging from 100 eV to 100keV, we note that, for X-ray Diffraction (XRD) applications, short wavelengths (hard x-rays) are used. These range from just a few angstroms (10^{-10}m) to 0.1 angstroms with energies ranging

from around 1keV to 120keV. Since these wavelengths are approximately the size of atoms, they are well suited for probing the structure of atoms and molecules in a vast array of materials. The energy of x-rays allows them to penetrate deep into the materials measured and yield information about the structure [13].

There two main ways in which x-rays are produced: 1) x-ray tubes, and 2) synchrotron radiation. In the first, x-ray tubes are generated by accelerating a focused electron beam through a high voltage field striking either a stationary or rotating target. As electrons slow down by colliding with the atoms in the target, a spectrum of x-rays are continuously released. This type of radiation is called Bremsstrahlung radiation. In atoms, the high energy electrons eject inner shell electrons through this ionization process. As free electrons fill the shells, an x-ray photon with energies characteristic of the material of the target is emitted. Copper and Molybdenum are two common targets for the x-ray tubes. The copper x-rays have energies around 8keV at a wavelength of 1.54 angstroms and molybdenum x-rays have energies 14keV at a wavelength of 0.8 angstroms. Energies of the x-ray photons is given by equation 3:

$$4. \quad E = \frac{hc}{\lambda}$$

In equation 1, E is the energy, h is called Plank's constant, c is the speed of light, and λ is the wavelength. The previously explained method is how x-rays are produced in laboratory instruments. The second method will be explained in more detail in the section on XAS.

In materials, the x-rays mainly interact with the electrons; when these x-ray photons and electrons collide, some of the incident beam photons are deflected away from the initial direction of travel. If there is no change in the wavelengths of the scattered x-rays (energy conservation), this is an elastic scattering process in which only the momentum has been changed called Thompson scattering. These types of x-rays are the ones measured in diffraction experiments, since the scattered x-rays contain information about the electron distribution in the measured material. In the other case (called Compton scattering), x-rays lose some of their energy to the electrons resulting in different wavelengths for the scattered x-rays than the incident ones.

Waves that are diffracted from different atoms can interfere with each other resulting in a strongly modulated intensity. When the atoms are arranged in a periodic manner, like crystals, the diffracted waves will yield sharp and distinct interference patterns with the same symmetry as the distribution of atoms. These will look like peaks in graphs of the data. Thus, measuring the diffraction pattern enables us to deduce the distribution of the atoms in the materials measured [13].

When x-rays are diffracted, there are a few possible outcomes which generate the peaks in the data. The first is when the intensities of the x-rays cancel each other out called destructive interference normally yielding no peaks. The second is when the intensities of the x-rays combine

or add together yielding constructive interference giving strong peaks. Lastly, and most frequently, a combination of the two results called partial interference yielding fuzzy looking peaks [14].

Now, XRD itself first started in 1912 when Max Von Laue discovered the fact that crystalline structures act like three dimensional diffraction gratings for x-rays with wavelengths similar to the spacing of the planes in crystal lattices. Today, X-Ray diffraction is a common technique used to study different crystal structures and atomic spacing. One of the many benefits of the technique is the reliance on basic principle physics, namely, Bragg's Law. Bragg's Law is satisfied when constructive interference or partial constructive interference occurs. Bragg's Law is given in equation 4:

$$2d \sin\theta = n\lambda \quad (5)$$

In equation 2, d is the distance between the charges (the planes or lattice spacing); n is an integer number and relates to the "order" of the reflection; λ is the wavelength of the x-ray beam. The lattice constant, d, aides in identifying the materials measured, and/or the direction, or plane, of the known measured material. The typical XRD convention, 2θ is the angle between the incoming and outgoing beam. There are many applications to XRD including: new material identification, crystal solution and refinement; determination of unit cell, bond-lengths, bond-angles and site-ordering; characterization of cation-anion coordination; variations in crystal lattice with chemistry; with specialized chambers, structures of high-pressures and/or temperatures phases can be determined; determination of crystal-chemical vs. environmental control on minerals; powder patterns can also be derived from single-crystals by the use of specialized cameras [15].

For this work, XRD was used to find the orientation of the sample using the peaks from the intensity at specific angles. This was achieved by knowing where the intensity peaks are expected for the material and measuring the grown samples in order to confirm growth along the desired direction.

An x-ray diffractometer consists of three basic components: an x-ray tube, a sample holder, and an x-ray detector. As explained earlier, the x-rays are generated in a cathode ray tube produce a spectra consisting of several components: the most common are K_α and K_β. K_α consists, in part, of $K_{\alpha 1}$ and $K_{\alpha 2}$. $K_{\alpha 1}$ has a slightly shorter wavelength but twice the intensity as $K_{\alpha 2}$. The exact wavelength are characteristic of the target material. In order to produce the needed monochromatic x-rays, it is necessary to filter using foils or crystals monochrometers. Because $K_{\alpha 1}$ and $K_{\alpha 2}$ are so close in wavelength, a weighted average of the two is used. Of the two common targets for x-ray production, mentioned above, Molybdenum is the typical material for single-crystal diffraction. These x-rays are collimated and directed onto the sample. As discussed before, once the geometry

of the impinging, incident x-rays satisfy the Bragg Equation (Equation 4), constructive interference occurs. The detector records and processes the x-ray signal and covert it to a count rate which is displayed on a device, usually a computer screen. The x-ray single crystal diffractometers use either a 3 or 4 circle goniometer, which is an instrument that measures angles or lets an object rotate to a precise angular position, these circles refer to the angles of 2θ, χ, φ, and ω which define the relationship between the crystal lattice, incident ray, and the detector. Samples are typically mounted on thin glass slides, then, mounted onto the goniometer head. Adjusting the X, Y, and Z orthogonal directions allows the sample to be centered within the x-ray beam. The x-rays travel through the collimator and are directed at the sample. X-rays are transmitted through the crystal reflected off the surface, or diffracted by the crystal lattice. The detector is protected by a beam stop located opposite to the collimator preventing burnout. The reflected rays are scattered away from the detector because of the angles, but, with the right orientation, they can be collected by the detector. In our modern diffractometers, they have a charge-coupled device which transform the detected x-ray photons into electrical signals sent to a computer. Crystal structures contain several thousand unique reflections with spatial arrangements called a diffraction pattern. The indices: h, k, and l may be assigned to each reflection, indicating the position within the pattern. The patterns have reciprocal Fourier transforms with relationships to the crystalline lattice structure and the real space unit cell. This is referred to as the solution to the crystal structure. Once the structure is solved, it is refined using the techniques of the least-squares [15].

In summary, x-ray diffraction is a method of measuring and investigating the properties of materials using an x-ray tube to generate the photons and bombarding the sample at specific angles in order to satisfy Bragg's Law. This yields valuable information which can be used to characterize different materials.

2.4 X-ray Absorption Spectroscopy

In 1897, Larmor was able to derive an equation for the total instantaneous power radiated from accelerated charged particles (equation 5).

$$6. \quad P = \frac{q^2 a^2}{6\pi\epsilon_0 c^2}$$

Where: P is the total power radiated; q is the charge; a is the acceleration; ϵ_0 is the permittivity of free space; and, c is the speed of light. About a year later, this formula was extended by Lienard yielding the equation (equation 6) for a relativistic particle undergoing centripetal acceleration in a circular trajectory.

$$7. \quad P = \frac{(\frac{E}{mc^2})^4}{R^2}$$

Where P is, again, the total power; E is the energy of the particle; m is the rest mass; c is the speed of light; and R is the radius of the trajectory. The fundamental principle that accelerated charges radiate is the foundation for synchrotron physics. But, after many years of development, in the

1940s, advances in accelerator technologies lead to the beginnings of our modern synchrotrons. Unfortunately, the realization of an actual synchrotron, and the basis for our modern facilities, would have to wait until the 1950s and 60s. It was then that the idea for a large ring used to store or house a continuously circulating beam of accelerated particles, simply, called storage rings [16]. Ever since its development, synchrotron based X-ray Absorption Spectroscopy (XAS) is a proven experimental method for studying the local environments of the cations in a multitude of materials. XAS yields information of the average interatomic distances, the number and chemical identities of neighboring atoms [17].

Because x-rays are ionizing radiation, synchrotrons are the best source for producing x-rays for XAS. The produced x-rays have sufficient energy to eject a core electron from an atom. These core shells have a specific binding energy, and, if the x-ray absorption is plotted as a function of energy, produce a spectrum for an atom resembling the spectrum for lead. As the x-ray energy is scanned through the binding energy of a core shell, there is a sudden increase in the absorption cross-section. This leads to the commonly referred to absorption edge, with each of the edges representing a different core-electron binding energy. These edges are named according to the principle quantum number of the electron being excited: K for n=1, L for n=2, M for n=3, etc. The binding energy for the core-electrons increase with increasing atomic number, from 284eV for the Carbon K edge to 115.606keV for the Uranium K edge, and the energies for L edges markedly lower than the corresponding K edges (e.g. the binding energy for the Uranium L_2 edge is 20.948keV and 17.166keV for the L_3 edge). XAS refers to the measurement of the x-ray absorption cross-section in the vicinity of one or more absorbing edges. For the most part, an absorption edge, by itself, is of little value except for identifying the element measured. However, if the edges are examined in more detail, they encapsulate a plethora of information. The absorption edge is not simply a discontinuous increase in the absorption, but, in fact, it shows the significant structure both in the immediate vicinity of the edge jump as well as above the edge. Sometime, the structure around the edge is referred to as the x-ray absorption near-edge structure. The oscillations above the edge are referred to as extended x-ray absorption fine structure. The difference between the two is arbitrary due to the fact that the same fundamental principles govern the photoabsorption over the whole XAS region. Therefore, there is no distinction between the near edge and the extended.

Now, the absorption of an ionizing x-ray is the result of the ejection of a photoelectron which leaves behind a highly excited core-hole state. There are a variety of mechanisms for the excited photoelectrons to relax back. The two most important being the emission of an Auger electron and x-ray fluorescence. Auger emission can be the dominant relaxation process for the lower energy states. X-ray fluorescence is the primary relaxation process for the higher energy excitation. Typically, x-ray fluorescence takes place in the K edge for elements with an atomic number greater than 40. For the even heavier elements, the spectrum is more complicated with a large number of emission lines. X-ray fluorescence has been around for longer than our modern and quantum understanding of this process. Therefore, there are no simple relationships between the names of

different emission lines and the origin of the line. Nevertheless, x-ray fluorescence is still governed by a series of selection rules which are referred to as "diagram lines." It must be kept in mind that other "forbidden" transition lines can also be observed which can also give important information. Interestingly, every element has its own unique x-ray emission energies which are usually well resolved from any neighboring emission lines.

If we start with the simplest case, the measurement of x-ray absorption spectrum only involves the measurement of the incident and transmitted flux. In order to minimize limitations, the measured XAS spectra are mostly the fluorescence excitation spectra. Equation 7 gives the expression for the reduction in intensity for the whether it is transmission or fluorescence.

$$8. \quad \mu x = \ln \frac{I_0}{I_1}$$

With μ being the linear absorption coefficient, which is determined by the atoms of the material; x is the thickness of the sample tested; I_0 is the x-rays incident upon the sample; and, I is the transmitted x-rays. If the variable I_0 was replaced to I_f, we would have the equation for the reduction by fluorescence [18].

Now, to complete our introduction on XAS, it is important to speak a little about x-ray absorption near edge structure (XANES). Although the energy of an absorption edge is not well defined, it still proves extremely useful when determining the oxidation state of the absorbing electron. For many years the energy edge increases as the oxidation of the state increases in the absorbing electrons. To explain this, it is necessary to consider the electrostatic model. Atoms with a higher oxidation state should, also, have higher charges which would, in turn, require higher energy x-rays to eject the core electrons. This gives a phenomenological relation between the edge energy and the oxidation state, and makes XAS extremely sensitive to oxidation states [18].

2.5 X-ray Magnetic Circular Dichroism

As mentioned before, XAS looks at the unoccupied states of electrons in the atoms. Furthermore, XAS seeks to analyze the integral unoccupied densities of the states vs. energy [19], specifically, of the k-integral measurements. Due to these integral measurements, XAS may determine magnetic moments similar to other material research methods. XAS is hyper sensitive and accounts for the disentanglement of spin and orbital magnetism, as well as probing the local atomic properties. Although XAS was discussed before, further discussion is necessary to help understand and explain X-ray Magnetic Circular Dichroism (XMCD). XMCD allows for the resolution of the element- and shell-selective magnetic properties to be measured.

Now, XAS is an umbrella term for many different form of spectroscopic measurements including: XANES, EXAFS, and, the object of this section, Dichroism in X-ray absorption with linearly polarized light which include: X-ray natural linear dichroism (XNLD), and X-ray magnetic linear dichroism (XMLD). When the light is circularly polarized, it results in two more classes of XAS, namely: X-ray natural circular dichroism (XNCD), and, finally, X-ray magnetic circular dichroism (XMCD) with XMCD being the focus of this section.

Dichroism is the polarization dependent absorption behavior. If a resultant charge or spin is directionally dependent (anisotropic) in a microscopic picture. When the dichroism is caused by a charge anisotropy, it is termed natural dichroism or a charge dichroism, but it is a magnetic dichroism if it is caused by an anisotropic spin distribution (Magnetism and Synchrotron Radiation) in the case of XNLD and XMCD. So, XMCD is produce when the charge anisotropy is caused by an axial spin alignment. In other words, x-ray magnetism circular dichroism is when a directionally dependent spin polarization behavior happens.

The first XMCD experiment was conducted in 1987 by Schütz et al. [20]. It is very good at providing simple evidence of an extrinsic origin of high temperature ferromagnetism. XMCD can, also, be understood as the difference of the x-ray absorption coefficient shown in equation 8:

$$9. \quad \mu_c = (\mu^- - \mu^+)$$

Where the orientation of the incident photon helicity and sample magnetization is given by μ^- for the antiparallel, and μ^+ for the parallel orientations. Specifically, XMCD is produced from a directional spin alignment that is even with respect to parity (sign does not change with spatial inversion) and odd with respect to time reversal (sign does change with time reversal). XMCD detects the independence of x-ray absorption on the helicity of the x-ray beam by a magnetic material. It is the difference between the $\Delta M = +1$ for left circular polarization and $\Delta M = -1$ for right polarization transitions (Magnetism and Synchrotron radiation). Therefore, XMCD is when an XAS spectrum is recorded with two specific conditions, namely, the light incident on the sample is circularly polarized, and the measured sample has some net magnetization. XAS and XMCD both have the same element and shell selectability properties through tuning the energies it is possible to select the transition (electron) to excite.

Furthermore, if polarized x-rays are used with XAS, additional selection rules come into play, thereby, lengthening the amount of information collected from XMCD (Relationship between Structure and Magnetic Behavior in ZnO Based Systems). Using the usual physics convention for right and left polarization, right circularly polarized light carries helicity (the angular momentum along the direction of propagation). This leads to absorption of right circularly polarized light

yielding transitions with Δm_j=+1 and Δm_j=-1 for left circularly polarized light. Thus, the dipole selection rules are as follows (Equation 9):

$$10.\ \Delta j = 0, \pm 1\ \ \Delta l = \pm 1\ \ \ \Delta s = 0\ \ and\ \ \Delta m_j = \pm 1$$

The last rule is at the origin for XMCD, and allows the extra selection rules to scan the difference in the density of empty states with different spin moment supplying magnetic information on the material of the sample measured. Using the two-step model from the 1987 experiment mentioned above [20], it is possible to give a qualitative understanding of XMCD. In step 1, a partially spin-polarized core electron is excited from an unpolarized initial core state [21] due to a circularly polarized photon. From the conservation of angular momentum in the absorption process, the photon's angular momentum is completely transferred to the photo-electron. Because of the lack of spin dependence, the spins of the electrons do not change except for when they are coupled to the orbital momenta by strong spin-orbit interactions. Ergo, both left circularly polarized and right circularly polarized light will excite half (50%) of the electrons with spin-up and the other half (50%) with spin-down if there is no connection with the spin and orbital part of the electron's angular momentum. The angular moment of the photon can be partially transferred to the spin by the spin-orbit coupling if a strong spin-orbit interaction is present. In this model, the photoelectrons are ejected with a polarization of the spin due to an imbalance between spin-up and spin-down excited electrons. Now the second step; the spin-polarized photoelectrons will detect the spin polarization of the final empty states while taking into account the Pauli Exclusion Principle. The XMCD will reflect the difference in the density of empty states with different spin moments. Also, in the second step, the magnetic properties of the sample will be measured because the spin-split valence shell will act like a detector for the spin of the excited photoelectrons.

The probability of a transition is proportional to the polarization of the electron and the spin-density differences. This probability can be express by equation 10:

$$11.\ P_e \frac{\Delta\rho}{\rho} = \frac{\mu^-(E) - \mu^+(E)}{\mu^-(E) + \mu^+(E)}$$

Where P_e is the electron polarization, ρ is the spin density, and $\Delta\rho = \rho\uparrow - \rho\downarrow$; also, $\rho\uparrow$ and $\rho\downarrow$ are the majority and minority like final state densities [19]. To fully clarify this idea, take the case of the $L_{2,3}$-edge spectrum of XMCD (i.e. 2p→3d transition) of any 3d transition metal [19]. It begins when the core electrons are excited by the circularly-polarized photon from its initial $2p_{3/2}$ (the L_3-edge) and $2p_{1/2}$ (L_2-edge) which are characterized by the quantum numbers j and m_j with j = l + s and j = l – s, respectively. No spin-orbit splitting and the exchange interaction splits the band into its spin-up spin-down components, due to the Stoner model assumption, for the final 3d states. This will lead to five degenerate spin-up states with density of states $\rho\uparrow$ and, also, five degenerate spin-down states with the density of states $\rho\downarrow$.

To finish this section, it is important to discuss some of the experimental pieces of XMCD in order to further understand this technique. There are two different way in which to perform XMCD experiments; by changing the helicity and holding the orientation of the magnetic field constant, or by changing the direction of the magnetic field and keeping the helicity constant. This is because, as mentioned earlier, the spectrum for XMCD is obtained as the difference of the absorption coefficient (equation 8) with μ^+ for the parallel and μ^- for the antiparallel orientations of the helicity for the photons and magnetic field applied to the sample. After collection, normalization, and subtraction of the μ^+ and μ^- spectrum, the spectrum for the XMCD is obtained. Depending on the beamline used, the time for processes of collection, normalization, and subtraction are shorter due to differing techniques.

Chapter 3: Analysis of LMO/STO Growth [51]

3.1 Introduction

Numerous studies have emerged on the observation of interfacial electronic reconstruction, and new electronic phases at both polar and non-polar interfaces in oxide materials [52 – 54]. Many factors contribute to the nature of the electronic reconstruction. Two of these include interfacial band alignment and the conductivity of the materials, which can alter the boundary conditions leading to the degree of charge compensation [55]. In general, any change in valence that results from the interfacial polar mismatch is what is used in this work. $LaAlO_3$ (LAO)/STO is one of the most widely studied systems of this kind [56]. The insulator $LaAlO_3$ has a band gap of 5.6eV which has alternating charged $(La)^+$ and $(AlO_2)^-$ alternating layer lying along the [001] direction. Additionally, the insulator STO has a band gap of 3.2eV consisting of neutral $(SrO)^0$ and $(TiO)^0$ alternating layers along the [001] direction. A polarization catastrophe is theorized to occur when these materials are together due to a potential buildup in the LAO polar layers driving a charge transfer from the LAO valence band to the STO conduction band in the LAO at a critical thickness of 4 unit cells [57 – 59]. This results in the STO being electron doped near the interface, thus, inducing a reduction of Ti^{4+} towards the Ti^{3+} [60] with an onset of conductivity [53]. Furthermore, other exotic interfacial phenomena have been observed including: orbital reconstruction [61], ferromagnetism [62], and superconductivity [63] with researchers investigating the role of structural imperfections in the effects at these interfaces [64 – 68].

With the initial observations of these interesting emergent phenomena at the heterointerface of LAO/STO, numerous additional systems have been found to replicate similar potential buildups induced by electronic reconstruction and other interfacial phenomena [71]. Additional studies relating to the polar and non-polar interfaces; mostly, $LaCrO_3$/STO [72], and $LaMnO_3$/STO [73]; suggest this rule may not actually be universal because no critical-thickness for metal-to-insulator transitions have been found in either system. Initially, this may be surprising because LMO is alternating $(LaO)^+$ and $(MnO_2)^-$ layers (Figure 3.1) with electronic reconstruction similar to that of the LAO/STO is expected to occur. At first, the absence of metallic conductivity was discouraging to researcher from continued study, but it does not expressly mean that interfacial polar mismatch is not influenced by charge or spin degrees of freedom. To the contrary, recent reports on the LMO/STO systems proposed charge transfers can actually happen within the LMO because of similar potential buildup produced by the electron doping near the interface and, also, due to the hole doping near the surface yielding ferromagnetism in LMO [74,75]. This does not mean, however, that direct evidence of electron reconstruction and the nature of magnetism is reported without a deeper understanding and control of functional properties.

Using XAS and XMCD along with some first principle calculations in order to study the effect of polar mismatch on the electric and magnetic structure of the polar and antiferromagnetic insulator

LMO which was grown on the nonpolar STO, a striking change in the Mn valence state of the LMO even down to a 2-unit cell thick film discovered with XAS, but the Ti valence of the STO was unchanged. Ferromagnetism was seen by XMCD at a critical thickness of 5 unit cells. As suggested by the decoupling of the charge, the magnetic ferromagnetism thickness, and the absence of the hole doping near the surface of the film, infer the charge transfer picture [74,75] may not be directly applicable or may be too simple of an explanation. In the theoretical studies, the potential buildup in the LMO is 0.177 V/Å, along with the small band gap of the LMO, leads in a critical thickness for the built in potential to fail in a 2-unit cell sample. Additionally, a chemical route was identified to effectively manipulate the doping level and modulate the influence in the polar mismatch in order to induce the ferromagnetism in the films to as low as 3 unit cells.

3.2 Substrate Treatment

Perovskites

STO and $NdGaO_3$ (NGO) are both perovskite oxides of the form ABO_3. The perovskite crystals, the A and B cations, are usually rare-earth or transition metals accompanied by oxygen anions. Ideally, the cubic structure can be described by networks of corner-sharing oxygen BO_6 octahedra with the oxygen atoms at the faces of the unit cell (Figure 3.2a), the A-site cations at the corners and the others, the B-site cations, at the center. The perovskite family of elements are named after a Russian statesman and mineralogist [29], Lev Perovski. Since it was discovered, perovskite materials have been greatly studied, and are usually quite common and familiar to materials researchers. They have a wealth of application from environmental [30], energy production [31], and communications [32]. The most common perovskites are slightly distorted from the ideal cubic shape, due to a non-ideal relative ration between the A and B ion sizes (Figure 3.2b). This results in a tetragonal or orthorhombic structure (Figure 3.2a). Since not all of these can be readily made into single crystals, it is possible to use PLD to synthesize many types of them into thin films [33]. STO, on the other hand, is readily available in single crystal substrates making, but must be treated for a better platform for certain types of growth (see Figure 3.2c).

Perovskites with a B site transition metal display a large variety of interesting magnetic and/or electronic properties. This flexibility arises from chemical properties, and the complexity of the character of transition metal ions. In transition metal oxides, it is normally the unfilled 3d electron shells that are related to the magnetic and electronic correlations with the filled 3d electron shells dealing primarily with the dielectric properties. The coexistence of random ferroelectric and ferromagnetic moments, called multiferrocity, is an elusive entity because of the small concentrations of the low-symmetry magnetic point groups which allow for the needed spontaneous polarization [34]. Despite this, large magneto-capacitive couplings were reported with the existence of competing interactions [35], canted moments [36, 37], and in composites [38].

With its high dielectric permittivity STO, specifically, is one of the perovskite materials which falls under the dielectric and ferroelectric categories; it is highly studied and mostly ferroelectric. The embryonic ferroelectrics may be terms as nearly ferroelectric crystals [39] which STO is an example. Significant quantum fluctuations of ions stifle the phase-transitions and lead them to a ferroelectric state and also maintain the soft transverse optical mode of the material. A divergence in the limit T to 0K along with the noticeable phonon anharmonicities [40] is displayed by the dielectric susceptibility. With these types of material systems, even trivial substitutions or doping may induce ferroelectric phase transitions. STO has a lattice of alternating SrO, and TiO_2 layers. This leads neutral structure with neutral layers.

NGO is also a perovskite structured material, as such, it also has the layered structure. It is the only lanthanide gallate oxide without structural phase transitions below 1000°C. As such, it is most often used for growth thin films that are twin-free and grown at lower phase transition temperatures [41]. Unlike STO, NGO is more suitable to microwave applications [42]. Various measurements revealed that NGO's layered structure is actually a distorted perovskite with an orthorhombic symmetry at room temperature [43-45]. NGO has a lattice of alternating NdO, and GaO_2 layers, but, unlike STO, NGO's layers are not neutral. They alternated with +1 and – 1 configuration. Do to these alternating layers, it is necessary to treat the substrates, both the NGO and the STO. These treatment procedures help remove any mixed termination, which exists on the substrate surface. In addition, the treatment ensures that the substrates are clean and free from any surface impurities. Furthermore, the importance of this will be understood during the discussion of the LMO growth and analysis in the experimental details section of this chapter.

Treatment of STO

STO consists of alternating layers of SrO, and TiO_2 has the most intensive treatment procedure of all of the substrates treated in this work. It begins with either a cleaning of the as received substrates or directly immersed in the Buffered Oxide Etch (BOE) solution which consists of Ammonium Fluoride – 30 – 40%, and Hydrofluoric – 1 – 5%, and stirred followed by immersion, and continued stirring in deionized water (DI). Following the BOE and DI, the substrates are dried with nitrogen (N_2) and placed in a ceramic holder (boat). Once in the boat, they are placed in to a tube furnace, and annealed at 1,050°C for 2 hours in an air environment (Figure 3.2). Following the treatment, the substrates were scanned with the AFM. In each treatment, no more than three substrates were treated at a time. This was more of a preference and helped to ensure the quality of every substrate treated.

Treatment of NGO

The NGO substrates have alternating NdO, and GaO_2 layers with a need for the them to be terminated on the GaO_2 layer. In order to achieve the highest quality single terminated substrates, a procedure similar to that of the STO was tested, due to the similar perovskite structure. Along with the procedure of the STO substrates other variations were tried involving treatments with and without the BOE. All of the NGO substrates were all initially cleaned with acetone and isopropyl alcohol, in an ultrasonic bath, before being place in the ceramic boat and annealed at 1,100°C for three hours in an air environment (Figure 3.3). Additionally, the treatment for NGO is not as "standard" as the procedure for STO and required varying the temperature, gas used, and anneal time to get the ideal procedure for treatment (See Table 3.1).

Conclusion for the substrate treatment

As can be seen from the AFM images (Figures 3.3 – 3.4), the treatment procedures all produced singly terminated terraced surfaces. This method of treatment is extremely effective at producing very high quality singly terminated substrates as shown in the figures. In fact, for the treated STO substrates, it was very rare for the listed procedures to not obtain the desired singly terminated surfaces on the substrates. Even though NGO and STO are both perovskite materials, the NGO substrates did not need the BOE step for their treatment procedure.

3.3 Experimental Details

The growth of the LMO films on the TiO_2 terminated STO along the (001) substrates were done using PLD with the assistance of RHEED [76]. The intensity of the RHEED oscillations were consistent throughout the growth, thus, indicating layer-by-layer growth for each sample [76]. Additional characterizations of the LMO heterostructures proved that they were, indeed, high quality with atomically with smooth surfaces, highly crystalline with dislocation free interfaces [76]. In order to investigate the potentials for electron reconstruction and the associated ferromagnetic order, soft XAS and XMCD was carried out at grazing incidence with total electron yield geometry on numerous LMO/STO heterostructures (Figure 3.5a paper below) [76]. When the samples were compared to the previous local magnetometry using a superconducting quantum interference device (SQUID) [74, 75], the current approach is sensitive to the surface providing a direct measurement of the valence states of the various elements in the films, and also the substrates, using XAS and allows the detections of the weak (~0.005 μ_B/atom), and element specific, magnetic moments which exclude any magnetic impurities with the XMCD [60]. Edges from the Mn $L_{2,3}$ at 25K showed the strong dichroism (Figure 3.5a) from the XMCD, indicate a net ferromagnetic moment coming from the Mn in the films. Noting some of the important conclusions are: the ability to detect the small magnetic moments of the 5 unit cells films; this is due to the XMCD sensitivity which were not seen in previous studies [74]. Next, the XMCD of the films as thin as 9 unit cells of the LMO are similar to those seen in hole doped $La_{0.67}Sr_{0.33}MnO_3$ [91].

Since XMCD is dependent on thickness, these results confirm the existence of intrinsic magnetization in the LMO films coinciding with previously conducted magnetometry studies [74, 75]. To further understand the nature of magnetism, XAS was conducted at both the Ti- and Mn-$L_{2,3}$ edges as a function of the LMO thickness, and the Ti-$L_{2,3}$ edges were unaltered and matched the STO substrate reference (Figure 3.5b). To state this another way, no sign of electron transfer to the STO and the bulk-like character of the Ti^{4+} was maintained at the LMO/STO heterointerface. Conversely, studies using XAS at the Mn-$L_{2,3}$ edges showed greater variation with the thickness of the films (Figure 3.5c). The electron transfer occurs at even the 3-unit cell sample. Additionally, it is expected for the valence state of the L_3 edge to be $Mn^{3.5+}$ due to the electron transfer, but this is not the case, as can be seen even down to the 3-unit cell sample, the valence state shifts from the expected state of $Mn^{3.5+}$ to a $Mn^{2.5+}$ state. (Figure 3.6c).

In order to explain this change in the Mn valence state, the spectra for bulk $SrMnO_3$ (i.e. Mn^{4+} reference), LMO (i.e. Mn^{3+} reference), and the MnO (i.e. Mn^{2+} reference) are provided for comparison [92, 93]. The relatively thick (12-unit cell) LMO films had an absorption spectra similar to that of the bulk LMO, thus, indicating a dominating Mn^{3+} valence state while noting that the absorption peak has a slightly lower energy position than the bulk LMO. This infers that the films are lightly electron doped. In the smaller (9-unit cell) LMO, the main spectral feature, near the 641.4eV, shifted toward lower energies showing an average lower valence state. For the even smaller films (6, 5, and 3-unit cell) films, there were even further shifts in the feature. Therefore, a prominent feature near the 640eV seems to correspond to the main absorption peak of the Mn^{2+}. It is important to, quickly, note that the suppression of the fine feature (~638eV) in the ultrathin LMO film, compared to the MnO reference spectrum, is probably because of the different local environments of the two structures [94]. If these results are compared with those of the 2-unit cell heterostructures, it is shown that the XAS spectrum has an absorption peak around the 639.8eV peak analogous to the Mn^{2+} (Figure 3.6). This strong Mn^{2+} peak in the 2-unit cell sample conveys an electronic reorganization happened which coincides with theoretical calculations; this is not included in the same graph because of some charging in the sample which distorts the spectral background. Nevertheless, the XAS clearly demonstrates a reduction in the average Mn valence state of the thin samples, thus, further concluding that electrons are accumulated in the LMO layers near the interface starting with the critical thickness of the 2-unit cell. Clearly, contrasting the XMCD studies described above and in the previous local magnetometry studies [74, 75], which concluded the emergent ferromagnetism is not detected for thicknesses below the 5 or 6-unit cell. Therefore, a decoupling of the electron accumulation and ferromagnetic critical thicknesses must occur.

The total electron yield geometry completed this study which scans the uppermost 3-5 nm of thin film samples in a way that the deeper layers can be neglected due to the exponential decay in the intensity with the distance from the film surface. Thus, as the thickness of the LMO increases, the contribution of the Mn at the interface will decrease as well. The valence state is likely non-uniform along the surface normal due to the observed decrease in the Mn^{2+} signatures in the Mn XAS spectrum with increasing LMO layer thickness. This leads to the fact that the fraction of Mn^{2+} is higher in the thinner films when contributions from the interface are more to the Mn XAS signal. As can be seen in Figure 3.7, it is evident that valence state of the O K edge evolves with the film thickness. There is also a possibility of the bottom 3-unit cell, near the interfacial region, stays rich in Mn^{2+} for the 5 and 6-unit cell sample [95]. When the sample thickness is larger than the 6-unit cell, it is comparable or larger than the scanning depth and region of the interface to the spectrum is lowered. In order to correct for the polar field, the interface will mostly build up excessive electrons, making an inhomogeneous charge profile through the thickness of the film. Fortunately, this coincides with other $La_{1-x}Sr_xMnO_3$/STO (001) heterostructures with excessive electrons accumulating up near the interfaces [95].

Other XAS studies of LMO/STO (001)o (where the O subscript designates an orthorhombic index) corroborating the accumulations of electrons due to polar mismatch can also be found. Treated NGO substrates produced GaO_2-terminated surfaces which are naturally polar [96], thus, there should not be any polar mismatch at the heterointerface of the LMO/NGO samples. Mn-$L_{2,3}$ edges are characteristic of the bulk like Mn^{3+} with no Mn^{2+} features from the XAS spectra. This is true even for the 3-unit cell thick films, and they are not dependent on thickness in the XAS spectra (Figure 3.5d); therefore, excess charges are not seen in the LMO/NGO heterostructures. Thus indicating that electrons accumulate on the LMO samples near the interfaces to reduce the polar catastrophe in LMO/STO heterostructures at the thin 2-unit cell thickness films.

To help explain the polarization catastrophe, we can think of the think of the layers of the LMO on STO as charged planes. The STO planes are charge neutral (i.e. no charge), but the LMO alternates between a charge of +1 and –1. This will turn them into a series of parallel plate capacitors. As more LMO layers are added, there is an increase in the potential of the system, which could, eventually, lead to an infinite potential build up. At some point, the material will contain this potential leading to the catastrophe. Because this cannot occur, the laws of nature step in, luckily, and averts this catastrophe. In order to do this, a half electron will have to transfer from the upper most layer (top) to the bottom layer (Figure 3.8). At some thickness it will this transfer will occur and it is called the critical thickness. The question is: when will this happen? Essentially, the band gap tells you how many layers, or capacitors are allowed before nature takes over. You must understand why you have to move the electron to the LMO layer. The electron has to move to the bottom layer of the LMO sample. If the electron does not transfer, you will have an infinite series of charges which cannot occur in nature. Due to this phenomena, nature steps in to fix it, and an electron is transferred from the top layer of LMO to the bottom layer of LMO. This effectively averts the catastrophe. Using this understanding and combining this with the large

difference in the band gap between LMO (1.3eV) and STO (3.2eV) [76] will result in a band configuration straddling the LMO/STO interface (Figure 3.8). Using these facts, it is expected that the electron accumulation will occur when the built in potential in the LMO layer overcomes the LMO band gap, by calculation, it should happen at a critical thickness of ~7.3 Å (a little shy of the 2-unit cell of LMO). The system becomes unstable and a way must be found to compensate the potential due to the results discussed just before. Due to the positive potential difference from the interface to the surface, a screening or a compensation effect will always lead the negative charges to build up near the interface. Naturally, this gives a reason for the reduction in the Mn^{3+} towards the Mn^{2+} at the very thin limit and near the interfaces for the thicker samples. This differs from the case of LAO/STO because the LAO band gap borders the STO bands with the negative charges staying in the STO near the interface and reducing the Ti^{4+} to the Ti^{3+} [58 – 60].

There was no indication of Mn^{4+} begin detected on or around the LMO film surfaces, interestingly, this implies that the charge transfer model [74, 75], proposed earlier, may well be an oversimplification or could possibly not be directly applicable to this system. Therefore, almost any number of additional surfaces, either structural or chemical, reconstructions might actually occur to recoup the electron accumulation [97 – 100]. Moreover, oxygen vacancies, especially, were considered as a way to offset the polar field [99 – 101]. With these LMO/STO heterostructures, no sign was given for the reduction and the vacancy formation of the oxygen in the STO because no signature of the Ti^{3+} was observed by the XAS near the interfaces and the heterostructures showed an insulating behavior [76]. By the same token, there was no indication for a large concentration of oxygen vacancies in both the film and substrate which resulted from the growths. The absence of evidence of Mn^{2+} in LMO/NGO heterostructures supports this which, even though they were grown at the same conditions, holds no evidence for a change in the valence state. These two indications are consistent for a high oxygen growth pressure (10^{-2}mbar) [76]. Furthermore, the appearance of Mn^{2+} in the LMO/STO heterostructures are associated with the polar discontinuity at the heterointerface regardless of the mechanism causing the accumulation of the electrons whether electronic, structural, and/or chemical in nature [97 – 102]. It was proposed that the oxygen vacancies, the vacancies not necessarily induced by the deposition process, may be an inherent compensation mechanism for polar/nonpolar oxide heterostructures possibly leading to an electron buildup at the interface [99, 100, 102].

In bulk, the stoichiometric LMO with Mn^{3+} is an A-type antiferromagnetic insulator [103]. Even with the possibility of electron-hole asymmetry in the manganite phase diagram similar to the cuprate family [104], adding extra holes or extra electrons with chemical doping may cause ferromagnetism due to the Mn^{3+} -O^{2-} -Mn^{2+} double exchange [103, 105-108]. The known extrinsic defects, cation-deficiency (e.g. La-deficiency) or excess oxygen, may also cause the ferromagnetism in LMO [109, 110]. Although, the deficient LMO is usually a ferromagnetic metal, whether cation deficient or oxygen excess, with a mixture of Mn^{3+} and Mn^{4+} (i.e. hole doping) [111]. This is not in line with the observations that the films were electron doped with standard cation stoichiometry and insulating behavior [76]. Thus, the appearance of electron doping, discuss

here, at the LMO/STO interface caused by the polar mismatch yields a valence mix (i.e. Mn^{2+}/Mn^{3+}) which is believed to result in the ferromagnetic phase [103, 105 – 108]. Indeed, the spectra seen in both XAS and XMCD in the relatively thick LMO/STO heterostructures (Figure. 3.5a,c) are akin to those of electron-doped manganites derived from the chemical effects of chemical alloying (e.g. Ce-doped LMO); these also show ground state that is insulating and ferromagnetic [108].

Films with less than 5 unit cells are void of ferromagnetism possibly because of "over accumulation" of Mn^{2+} (coming from large numbers of electrons needing to make room for the potential and coming from a reduction in magnetization from a lack of double-exchange coupling with Mn^{3+}); this tends to an antiferromagnetic state [106]. Consequently, the likelihood of lowering the Mn^{2+} inherent composition of the films was investigated to comprehend the source of the ferromagnetism and demonstrating the potential of these systems. Other studies found La-vacancies yield hole doping in LMO [109, 111]. For this reason, the 5% La-deficient LMO ($La_{0.95}MnO_3$) films were grown with varying thicknesses on STO substrates [76] in order to generate holes that should counter-dope the system under the influence of the potential and alleviate the amount of Mn^{2+} in the ultra-thin films (i.e., lower an over-electron-doped state to an "optimally-doped" state). This is an adequate path to introduce holes into the LMO using the defect formula (equation 12):

$$12.\ (La^{3+}_{1-x})[V^{3-}_{La}]_x(Mn^{3+}_{1-3x}Mn^{4+}_{3x})O^{2-}_3.$$

Now, the $La_{0.95}MnO_3$ shows an alternating $(La_{1-x}O)^{1-3x}$ and $(Mn^{3+}_{1-3x}Mn^{4+}_{3x}O_2)^{-1+3x}$ layers and, therefore, a polar mismatch still exists at the $La_{0.95}MnO_3$/STO interface. Because of the La-deficiency, a reduction is produced in the magnitude of the polar discontinuity with additional holes. The observed weaker thickness dependence of the Mn valence of the $La_{0.95}MnO_3$ films from the XAS (Figure 3.9a). The peak corresponding to Mn^{2+} at 639.8eV, specifically, is suppressed in the 3-unit cell thick $La_{0.95}MnO_3$/STO heterstructures (Figure 3.9b). This affirms the significance of regulating the valence state of the material to alleviate the over accumulation of electrons. Altogether, the examination of an insulating ferromagnetic ground state in films as thin as just 3 unit cells illustrates the capability to grow and measure emergent phenomena at interfaces, and has the potential applications in spin polarized tunneling devices.

In order to encapsulate, there is explicit corroboration for electron accumulation and ferromagnetism arising within the polar, antiferromagnetic insulator LMO when it is grown on the non-polar STO. Armed with first-principle calculations, and XAS, the critical thickness for the dawning of electron accumulation is determined to be the 2-unit cell. "Over-doping" of the LMO can be driven by the strength of the polar mismatch which the onset of ferromagnetism has contained as the average valence state dips towards Mn^{2+}. Ferromagnetism is noticed in only the 5-unit cell thick films in the stoichiometric LMO. This is led by the chemical doping (attained by

the control of the film stoichiometry), the average valence state can be adjusted, and obvious ferromagnetism may be seen in $La_{0.95}MnO_3$ films as thin as 3 unit cells. Finally, this exhibits the state-of-the-art referring to ultra-fine controls of materials, through which governing the atomic-structure of interfaces and the doping levels, extraordinary properties and control of material is obtained.

Chapter 4: Experiment Details and Procedure

4.1 Introduction

With the goal of growing a $Y_2Ti_2O_7$ sample along the (111) direction, a test sample was grown (sample 1). For a base line, the growth conditions were followed for a similarly structured pyrochlore material [112]. Reflectivity measurements were conducted to verify growth, and to ascertain the thickness of the sample. If the thickness is known, in nanometers, as well as the number of pulses, the rate of growth per pulse can be calculated (equation 13). While the growth was successful, the sample was not grown along the desired direction, or, in other words, it was not grown at the desired phase.

$$13.\ G_r = \frac{F_t}{N_p}$$

Where G_r is the growth rate, F_t is the film thickness, N_p is the number of pulses. Once the growth rate is obtained, it is possible to grow any sized sample based on the number of pulses. After this, the next step was to vary some of the growth conditions to discover the best environment for YTO (111) growth. Growth pressure and temperature were the variables used to figure out the ideal conditions.

Yttrium Stabilized Zirconium

The Yttrium Stabilized Zirconium (YSZ) is similar to the STO treatment, but without the BOE steps. In place of the BOE parts, it is cleaned, as all of the others, in acetone and isopropyl alcohol in an ultrasonic bath; then, they were annealed at 1,050°C for 2 hours in air.

The YSZ substrates produced the desired single terminated and terraced surfaces (Figure 4.1), but with rougher and more jagged edges than the STO and NGO substrates. Despite the rougher edges, the treated YSZ substrates were still sufficiently terraced for future growths.

4.2 Set up

We started with a single crystal YTO (227) grown at the University of Tennessee that was cut into two pieces. We attached one of the pieces onto a round stainless steel target holder with carbon tape and placed onto a rotating carousel. Before each growth, the YTO target was sanded in a “figure 8” pattern until a smooth and uniform surface was achieved and all of the remnants of the previous growth removed. All of the substrates were attached to the plate for growth using silver paint and cured for 20 minutes at 120° F. The preablation was done at 500 to 2000 pulses at 2Hz

depending on how long it was since the last growth to ensure a uniform target by removing any possible imperfections.

4.3 Growth conditions

In total, 15 Samples were grown at varying temperatures and pressures, but all of the samples were grown using the large mask (3mm x 16mm), the laser set at 18.0kV to 19.5kV to achieve an average fluency of 4.166 J/cm^2. In order to determine the most ideal growth conditions, the samples were grown at the following pressures: 0.013mbar, 0.0667mbar, and 0.133mbar with temperature of: 600 to 800° C at 50° intervals for a total of 15 samples. The current and power for the laser heater ranged from 11W to 27W and 4A to 6.7A respectively. Furthermore, all samples were grown with 2000 pulses at 2Hz and cooled down to room temperature at 15°/min at growth pressure (See Table 4.1).

4.4 Analysis of growths and data

To place the data into prospective and assist in understanding, the XRD data shows the intensity of the x-ray beam as a function of angle (called 2θ); sharp, or strong, peaks are produced when Bragg's law is satisfied as described above in chapter 2. The phases that are grown will have peaks at certain angles and are specific characteristics of the material grown. These properties are usually known or can be calculated, if not known. This tells us which of the phases of the sample were grown, or the direction of growth. To elaborate some more details from chapter 2, the spacing between unit cell layers is called the d spacing. The different phases are based on the lengths of the d spacing. In the YTO (111) case, the d spacing along the (111) direction (Figure 4.3) is longer than the d spacing for any other YTO phase with d = 5.82523 Å. If we know this to be the value for d, solving equation 4 (with d = 5.82523 Å, λ = 1.54 Å, and n = 1 and n = 2) for the angles yield peaks at 2θ ≈ 15.2°, and 30.7° for (111) phase and the (222) phase respectively. Therefore, peaks are expected at these angles for the YTO samples. Additionally, there should be a peak at 2θ = 30° for the YSZ substrate.

An initial review of the data reveals peaks at the 30° angle for all samples grown (Figure 4.2). Furthermore, a peak at the 31° angle appears in all of the samples grown at 700°C to 800°C (Figure 4.2, also Figures 4.6 & 4.7). Finally, there is a small peak at the 15.52° angle. The peak at 30° angle is, most likely, from the substrate (bottom plot in Figure 4.2, also Figure 4.7) and is expected to be present for all of the samples grown. There is nothing particularly distinctive about the samples grown from 600°C to 650°C; they all still have the expected peak at the 30° angle (Figure 4.4), but no other peak is observed; thus, indicating that no phases of YTO or Y_2O_3 were grown. For all of the samples grown from 700°C to 800°C, a clear peak appears at the 31.5° angle. This peak denotes a possible YTO (222) phase, but could, also, be a growth of Y_2O_3 on the substrate; instead of the desired YTO (222) phase. Although, the possible growth of a Y_2O_3 phase was, subsequently, ruled out due to lack of evidence in the XRD data. The growth of Y_2O_3 further

omitted due to its small d spacing. The 800°C samples have the peaks at angles: 30°, 31°, and an additional peak at the 15.52° angle. The peak at the 15.52° angle is the peak with the desired YTO (111) phase (Figure 4.7). To further solidify the optimum temperature to be 800°C and pressure to be 0.0133mbar, the peak ratios were estimated. This aides in assurance of these conditions. As can be seen, the samples grown at 0.133mbar and 0.068mbar both have a small bump around the 15.52° angle, but the 0.0133mbar sample has the most prominent peak at this angle.

Further inspection of the data reveals the existence of a possible phase boundary lying somewhere between the 650°C to 700°C temperatures (Figure 4.5) due to the peak at the 31.5° angle, and can be seen in all of the samples grown at 700°C to 800°C. It is believed that the boundary is temperature dependent due to the existence of the peak at all of the growth pressures. At the 800°C temperature, our desired YTO (111) phase appears as well as the other phases which are present in the samples grown at 700°C to 750°C (Figure 4.6). The growth of the YTO (111) phase at this temperature reveals the more ideal growth conditions of 800°C at a pressure of 0.0133mbar (Figure 4.7). It is, also, important to note that all of the materials involved in the growth (YTO, YSZ, Y_2O_3) have phases around the 30°, and 31° angles. Thus, making it extremely difficult to differentiate which of the materials were actually grown or if all three materials are present in the samples grown from 700°C to 800°C (Figure 4.6, and Figure 4.7)

Chapter 5: Outlook and Further Experimental Work

5.1 LMO/STO summary and outlook

As illustrated in this work, material science is a fascinating field. All of the different experimental techniques give material's researchers plenty of tools to investigate the properties of the many different known materials while leaving room for improvement with the, seemingly, infinite number of possible material combinations. Leading to important discoveries in our understanding of the fundamental electronic properties of materials. Especially, that of LMO/STO where it was shown, among other things that the valence states of the Mn ions amazingly and simultaneously verify our theories and models as it also defies them. Thus, enabling the refinement of our understanding of nature and the laws of physics. Furthermore, it is interesting to note, the importance of the results of chapter 3. Where more work can be done to help understand the nature of the compensation of the valence electron states in the LMO/STO materials and the shift in the magnetic properties of those types of samples. Further illustrated, there is definitive evidence for the accumulation of electrons and the ferromagnetism stemming inside LMO causing a polar, and antiferromagnetic insulator when the material is grown on the non-polar STO. Through the use of first-principle calculations, and XAS, the critical thickness for the development of electron accumulation is determined to be at the 2-unit cell thick sample. As illustrated, the "Over-doping" of the LMO can be directed by the strength of the polar mismatch, which the commencement of ferromagnetism has contained as the average valence state shifts towards the Mn^{2+} state. Ferromagnetism was detected only in the 5-unit cell thick films in the stoichiometric LMO. The ferromagnetic characteristics are managed by the chemical doping, the average valence state can be adjusted, and distinct ferromagnetism may be seen in $La_{0.95}MnO_3$ films as thin as 3 unit cells. Furthermore, this state-of-the-art and ultra-fine control leads to extraordinary properties and an unprecedented control of the material is obtained.

5.2 YTO Growth summary and outlook

As with the LMO, the research into the growth of the YTO samples furthers our knowledge of the possible growth conditions of the desired (111) phase. The data from the growths show a possible phase boundary existing in the lower temperatures due to the possible (111) phase grown at 800° C. Since our initial sample growths did not produce the target phase, more samples were grown and the variation in the growth parameters were widened from a starting temperature of 700°C to a starting temperature of 600°C and the starting pressure from 0.133mbar to 0.0133mbar. This change was done in order to understand why the desired phase was not grown and to find the ideal growth conditions. This is due to the formation of the peaks around those temperatures, and at those angles, which is consistent across all of the different growth pressures, and due to the estimation of the peak ratios. The apparent ideal growth conditions will be around the 800° C, and at a pressure around 0.0133mbar. As briefly mentioned in chapter 1, our overarching goal was to grow a ZDSO frustrated magnet. To do this, we needed to lay a foundation for optimum growth.

We started substrate treatment and moved on to growing a YTO film for a more conducive environment for ZDSO growth. This buffer layer of YTO provides a better fit for the ZDSO due to the similar lattice match of the YTO and ZDSO. Some of the future work can include a continuation of this project by initial ZDSO samples grown on a buffer layer of YTO of a few nanometers using the growth conditions detailed in this work. Additional work can, also, be done to verify the ideal growth conditions revealed in this work.

Bibliography

1. S.A. Kramer, H. L. Tuller, Solid State ionics 82 (1995) 15, T. Norby, J. Mater, Chem. 11 (2001) 11
2. F.W. Shi, X.J. Meng, G.S. Wang, T. Lin, J.H. Ma, Y.W. Li, J.H. Chu, Phys. B: Condens. Matter 370 (2005) 277.
3. G.R. Lumpkin, M. Pruneda, S. Rios, K.L. Smith, K. Trachenko, K.R. Whittle, N.J. Zaluzec, J. Solid State Chem. 180 (2007) 1512.
4. R. Vassen, D. Sebold, D. Stoever, Ceram. Eng. Sci. Proc. 28 (2008) 27.
5. W. Ren, S. Trolier-McKinstry, C.A. Randall, T.R. Shrout, J. Appl. Phys. 89 (2001) 767.
6. B.J. Wuensch, K.W. Eberman, C. Heremans, E.M. Ku, P. Onnerud, E.M. Yeo, S.M. Haile, J.K. Stalick, J.D. Jorgensen, Solid State Ionics 129 (2000) 111.
7. R.C. Ewing, W.J. Weber, J. Lian, J. Appl. Phys. 95 (2004) 5949
8. Johnson, Michel & D. James, David & Bourque, Alex & A. Dabkowska, Hanna & D. Gaulin, Bruce & Anne White, Mary. (2009). Thermal properties of the pyrochlore, Y2Ti2O7. Journal of Solid State Chemistry. 182. 10.1016/j.jssc.2008.12.027.
9. Villain J 1979 Z.Phys. B 33 31
10. T. Bramwell, Steven & Gingras, M. (2001). Spin Ice State in Frustrated Magnetic Pyrochlore Materials. Science (New York, N.Y.). 294. 1495-501. 10.1126/science.1064761.
11. Binnig, Gerd & Quate, C.F. & Gerber, Ch. (1986). The Atomic Force Microscope. Physical Review Letters. 56. 930-933. 10.1103/PhysRevLett.56.930.
12. R. Wilson, H. Bullen 2006, Introduction to Scanning Probe Microscopy (SPM), Basic Theory Atomic Force Microscopy (AFM), (April 23, 2018) http://asdlib.org/onlineArticles/ecourseware/Bullen/SPMModule_BasicTheoryAFM.pdf

13. MRL Materials Research Laboratory at UCSB (2017), X-Ray Basics, http://www.mrl.ucsb.edu/centralfacilities/x-ray/basics (April 23, 2018)
14. Harding, Guide to Understanding X-Ray Crystallography, http://www.chem.ucla.edu/~harding/ec_tutorials/tutorial73.pdf, (April 23, 2018)
15. C. M. Clark, B. L. Dutrow, Single-crystal X-ray Diffraction, Geochemical Instrumentation and Analysis, https://serc.carleton.edu/research_education/geochemsheets/techniques/SXD.html (April 23, 2018)
16. Arthur Robinson, Section 2.2 History of Synchrotron Radiation, X-Ray Data Booklet, http://xdb.lbl.gov/Section2/Sec_2-2.html (April 23, 2018)
17. Gordon Brown, 1999, X-ray Absorption Spectroscopy: Introduction to Experimental Procedures, Molecular Environmental and Interface Science, http://www-ssrl.slac.stanford.edu/mes/xafs/xas_intro.html, (April 23, 2018)
18. Penner-Hahn, James E(May 2005) X-ray Absorption Spectroscopy. In: eLS. John Wiley & Sons Ltd, Chichester. http://www.els.net [doi: 10.1038/npg.els.0002984]
19. H. Wende, and C. Schmitz-Antoniak, 2010, X-Ray Magnetic Dichroism, in E. Beaurepaire, F. Scheurer, G. Krill, J.-P. Kappler, eds., *Magnetism and Synchrotron Radiation*, Springer, Berlin, pp. 145-167.
20. G. Schutz, W. Wagner, W. Wilhelm, P. Kienle, R. Zeller, R. Frahm, and G. Materlik, Phys.Rev. Lett. **58**, 737 (1987)
21. R. Nakajima, J. Stohr, Y.U. Idzerda, Phys. Rev. B **59**, 6421 (1999)
22. F. Breech, L. Cross: Appl. Spectrosc. **16**, 59 (1962)
23. R.E. Honig, J.R. Woolston: Appl. Phys. Lett. 2, 138 (1963)

24. J.C. Miller, R.F. Haglund, Jr. (eds.): *Laser Ablation Mechanisms and Applications*, Lect. Notes Phys., Vol. 389 (Springer, Berlin, Heidelberg 1991)

25. D. Dijkkamp, T. Venkatesan, X.D. Wu, S.A. Shaheen, N. Jisrawi, Y.H. Min-Lee, W.L. McLean, M. Croft: Appl. Phys. Lett. 51, 619 (1987)

X.D. Wu, D. Dijkkamp, S.B. Ogale, A. Inam, E.W. Chase, P.F. Micelli, C.C. Chang, J.M Tarascon, T. Venkatesan: Appl. Phys. Lett. 51, 861 (1987)

26. T. Venkatesan, X.D. Wu, A. Inam, J.B. Wachtman: Appl. Phys. Lett. 52, 908 (1988)

27. Koster, Gertjan. (1999). Artificially layered oxides by pulsed laser deposition. Energy for Sustainable Development.

28. J. Gonzalo, C.N. Afonso, J. Periere and R. Gomez San Roman, Appl. Surf. Sci. 96-98, 693 (1996)

29. N. Mathur and R.-M. Thomas, New Scientist 2 May, 31 (1998)

30. L. L. Hench, D. E. Clark, and A. B. Harker. Review: Nuclear waste solids. Journal of Materials Science, 21:1457–1478, 1986.

31. N. P. Brandon, S. Skinner, and B. C. H. Steele. Recent advances in materials for fuel cells. Annual Review of Materials Research, 33:183–213, 2003.

32. W. Piekarczyk, W. Weppner, and A. Rabenau. Dissociation pressure and gibbs energy of formation of Y3Fe5O12 and YFeO3. Materials Research Bulletin, 13: 1077–1083, 1978.

33. Kuiper, B 2014, Size effects in epitaxial oxide thin films, University of Twente, Enschede. DOI: 10.3990/1.9789036536097

34. H. Schmid, Ferroelectrics, 162, 317 (1994).

35. J. Hemberger, P. Lunkenheimer, R. Fichtl, H.A.K. von Nidda, V. Tsurkan, and A. Loidl, Nature 434, 364 (2005).

36. T. Kimura, T. Goto, H. Shintani, K. Ishizaka, T. Arima and Y. Tokura, Nature 426, 55 (2003).

37. D. Higashiyama, N. Kida, S. Miyasaka, T. Arima, and Y. Tokura, Phys. Rev. B 70, 174405 (2004).

38. H. Zheng, J. Wang, S. E. Lofland, Z. Ma, L. Mohaddes-Ardabili, T. Zhao, L. Salamanca-Riba, S. R. Shinde, S. B. Ogale, F. Bai, D. Viehland, Y. Jia, D. G. Schlom, M. Wuttig, A. Roytburd, and R. Ramesh, Science 303, 661 (2004).

39. U.T. Höchli, K. Knorr, and A. Loidl, Adv. Phys. 39, 405 (1990).

40. J.G. Bednorz, K.H. Müller, Phys. Rev. Lett. 52, 2289 (1984).

41. Cao L X, Zegenhagen J, Sozontov E and Cardona M 2000, Physica C 337 24

42. J.M. Phillips 1996 J. Appl. Phys. 79 1829 and references therein

43. M arezio, J.P. Remeika and P.D. Dernier 1968 *Inorg. Chem.* \ 1337: I. Utke, Klemenz C., Scheel H.J., Sasaura M. and Miyazawa S 1997 *J. Crystal Growth* 174 806; Vasylechko l., Matkovskii A., Savytskii D, Suchocki A and Wallrafen F 1999 *J. Alloys Compounds* 291 57

44. Marti W., Fischer P., Altorfer F., Scheel H.J. and Tadin M.J. 1994 *J. Phys.: Condes. Matter* 6 127

45. Vasylechko L., Akselrud L., Morgenroth W., Bismayer U., Matkovskii A., and Savtskii D. 200 *J. Alloys Compounds* 297 46

46. Haeni JH, Irvin P, Chang W et al 2004 Nature (London) 430 758

47. Choi KJ, Biegalski M, Li YL, Sharan A, Schubert J, Uecker R, Reiche P, Chen YB, Pan XQ, Gopalan V, Chen L-Q, Schlom DG, Eom CB 2004 Science 306 1005

48. Vasudevarao A, Kumar A, Tian L, Haeni JH, Li YL, Eklund C-J, Jia QX, Uecker R, Reiche P, Rabe KM, Chen LQ, Schlom DG, Gopalan V 2006 Phys. Rev. Lett. 97 257602

49. Catalan G, Janssens A, Rispens G, Csiszar S, Seeck O, Rijnders G, Blank DHA, Noheda B 2006 Phys. Rev. Lett. 96 127602

50. H. M. Christen, G. E. Jellison, I. Ohkubo, S. Huang, M. E. Reeves, E. Cicerrella, J. L. Freeouf, Y. Jia, and D. G. Schlom, Appl. Phys. Lett. **88**, 262906 (2006))

51. Chen, Zuhuang & Chen, Zhanghui & Q. Liu, Z & E. Holtz, M & Li, Changjian & Wang, Xian-Jun & Lv, Weiqiao & Motapothula, Mallikarjuna & S. Fan, L & A. Turcaud, J & R. Dedon, L & Frederick, C & J. Xu, R & Gao, R & T. NDiaye, A & Arenholz, E & Mundy, Julia & Venkatesan, T & A. Muller, D & W. Martin, L. (2017). Electron Accumulation and Emergent Magnetism in LaMnO3/SrTiO3 Heterostructures. Physical Review Letters. 119. 10.1103/PhysRevLett.119.156801.

52. A. Ohtomo, D.A. Muller, J. L. Grazul, H. Y. Hwang, Nature **419**, 378 (2002).

53. A. Ohtomo, H. Y. Hwang, Nature, **427**, 423 (2004).

54. H. Y. Hwang, Y. Iwasa, M. Kawasaki, B. Keimer, N. Nagaosa, Y. Tokura, Nat. Mater., **11**, 103 (2012).

55. H. Seungbum, M. N. Serge, & D. F. Dillon, Rep. Prog. Phys. **79**, 076501 (2016).

56. J. Mannhart, D. G. Schlom, Science, **327**, 1607 (2010).

57. S. Thiel, G. Hammerl, A. Schmehl, C. W. Schneider, J. Mannhart, Science, **313**, 1942, (2006).

58. J. Lee, A. A. Demkov, Phys. Rev. B **78**, 193104 (2008).

59. J. W. Park, D. F. Bogorin, C. Cen, D. A. Felker, Y. Zhang, C. T. Nelson, C. W. Bark, C. M. Folkman, X. Q. Pan, M. S. Rzchowski, J. Levy, C. B. Eom, Nat. Commun., **1**, 94 (2010).

60. J. S. Lee, Y. W. Xie, H. K. Sato, C. Bell, Y. Hikita, H. Y. Hwang, C.C. Kao, Nat. Mater., **12**, 703-706 (2013).

61. M. Salluzzo, J. C. Cezar, N. B. Brookes, V. Bisogni, G. M. De Luca, C. Richter, S. Thiel, J. Mannhart, M. Huijben, A. Brinkman, G. Rijnders, G. Ghiringhelli, Phys. Rev. Lett. **102**, 166804 (2009).

62. A. Brinkman, M. Huijben, M. van Zalk, J. Huijben, U. Zeitler, J. C. Maan, W. G. van der Wiel, G. Rijnders, D. H. A. Blank, H. Hilgenkamp, Nat. Mater., **6**, 493 (2007).

63. N. Reyren, S. Thiel, A. D. Caviglia, L. F. Kourkoutis, G. Hammerl, C. Richter, C. W. Schneider, T. Kopp, A. S. Ruetschi, D. Jaccard, M. Gabay, D. A. Muller, J. M. Triscone, J. Mannhart, Science, **317**, 1196 (2007).

64. W. Siemons, G. Koster, H. Yamamoto, W. A. Harrison, G. Lucovsky, T. H. Geballe, D. H. A. Blank, M.R. Beasley, Phys. Rev. Lett. **98**, 196802 (2007).

65. G. Herranz, M. Basletić, M. Bibes, C. Carrétéro, E. Tafra, E. Jacquet, K. Bouzehouane, C. Deranlot, A. Hamzić, J. M. Broto, A. Barthélémy, A. Fert, Phys. Rev. Lett. **98**, 216803 (2007).

66. S. A. Chambers, M. H. Engelhard, V. Shutthanandan, Z. Zhu, T. C. Droubay, L. Qiao, P. V. Sushko, T. Feng, H. D. Lee, T. Gustafsson, E. Garfunkel, A. B. Shah, J. M. Zuo, Q. M. Ramasse, Surf. Sci. Rep. **65**, 317 (2010).

67. E. Breckenfeld, N. Bronn, J. Karthik, A. R. Damodaran, S. Lee, N. Mason, L. W. Martin, Phys. Rev. Lett. **110**, 196804 (2013).

68. Z. Q. Liu, C. J. Li, W. M. Lü, X. H. Huang, Z. Huang, S. W. Zeng, X. P. Qiu, L. S. Huang, A. Annadi, J. S. Chen, J. M. D. Coey, T. Venkatesan, and Ariando, Phys. Rev. X **3**, 021010 (2013).

69. J. S. Kim, S. S. A. Seo, M. F. Chisholm, R. K. Kremer, H. U. Habermeier, B. Keimer, H.N. Lee, Phys. Rev. B **82**, 201407 (2010).

70. Y. Hotta, T. Susaki, H. Y. Hwang, Phys. Rev. Lett. **99**, 236805 (2007).

71. P. Xu, Y. Ayino, C. Cheng, V.S. Pribiag, R.B. Comes, P.V. Sushko, S.A. Chambers, B. Jalan, Phys. Rev. Lett. **117**, 106803(2016).

72. S.A. Chambers, L. Qiao, T.C. Droubay, T.C. Kaspar, B. W. Arey, P. V. Sushko, Phys. Rev. Lett. **107**, 206802 (2011).

73. P. Perna, D. Maccariello, M. Radovic, U. Scotti di Uccio, I. Pallecchi, M. Codda, D. Marré, C. Cantoni, J. Gazquez, M. Varela, S. J. Pennycook, F. M. Granozio, Appl. Phys. Lett. **97**, 152111 (2010).

74. X. R. Wang, C. J. Li, W. M. Lü, T. R. Paudel, D. P. Leusink, M. Hoek, N. Poccia, A. Vailionis, T. Venkatesan, J. M. D. Coey, E. Y. Tsymbal, Ariando, H. Hilgenkamp, Science **349**, 716 (2015).

75. Y. Anahory, L. Embon, C. J. Li, S. Banerjee, A. Meltzer, H. R. Naren, A. Yakovenko, J. Cuppens, Y. Myasoedov, M. L. Rappaport, M. E. Huber, K. Michaeli, T. Venkatesan, Ariando, E. Zeldov, Nat. Commun., **7**, 12566 (2016).

76. See supplementary material at http://link.aps.org/supplemental/ for details on films growth, structural characterization, soft X-ray absorption measurement, transport and magnetic properties characterizations, and first-principles calculations which includes Refs. [26-39].

77. L. F. Kourkoutis, J. H. Song, H. Y. Hwang, D. A. Muller, Proc. Natl. Acad. Sci. U.S.A. 107, 11682 (2010).

78. A. Tebano, C. Aruta, S. Sanna, P.G. Medaglia, G. Balestrino, A.A. Sidorenko, R. De Renzi, G. Ghiringhelli, L. Braicovich, V. Bisogni, N.B. Brookes, Phys. Rev. Lett. 100, 137401 (2008).

79. D. Pesquera, G. Herranz, A. Barla, E. Pellegrin, F. Bondino, E. Magnano, F. Sánchez, J. Fontcuberta, Nat Commun, 3, 1189 (2012).

80. D.-Y. Cho, S.J. Oh, D.G. Kim, A. Tanaka, J.H. Park, Phys. Rev. B 79, 035116 (2009).

81. M. Abbate, F.M.F. de Groot, J.C. Fuggle, A. Fujimori, O. Strebel, F. Lopez, M. Domke, G. Kaindl, G.A. Sawatzky, M. Takano, Y. Takeda, H. Eisaki, S. Uchida, Phys. Rev. B 46, 4511 (1992).

82. G. Subias, J. García, M. C. Sánchez, J. Blasco, and M. G. Proietti, Surf. Rev. Lett. 09, 1071 (2002).

83. P.E. Blöchl, Phys. Rev. B 50, 17953-17979 (1994).

84. G. Kresse, D. Joubert, Phys. Rev. B 59, 1758-1775 (1999).

85. G. Kresse, J. Hafner, Phys. Rev. B 47, 558-561 (1993).

86. G. Kresse, J. Furthmüller, Phys. Rev. B 54, 11169-11186 (1996).

87. J.P. Perdew, K. Burke, M. Ernzerhof, Phys. Rev. Lett. 77, 3865-3868 (1996).

88. H.J. Monkhorst, J.D. Pack, Phys. Rev. B 13, 5188-5192 (1976).

89. Y. Li, & J. Yu, *J. Appl. Phys.* **108**, 013701 (2010).

90. G. Singh-Bhalla, C. Bell, J. Ravichandran, W. Siemons, Y. Hikita, S. Salahuddin, A. F. Hebard, H. Y. Hwang, and R. Ramesh, *Nat Phys* **7**, 80-86, (2011).

91. F. Yang, M. Gu, E. Arenholz, N. D. Browning, Y. Takamura, J. Appl. Phys. **111**, 013911 (2012).

92. C. Mitra, Z. Hu, P. Raychaudhuri, S. Wirth, S.I. Csiszar, H.H. Hsieh, H.J. Lin, C.T. Chen, L.H. Tjeng, Phys. Rev. B **67**, 092404 (2003).

93. T. Burnus, Z. Hu, H. H. Hsieh, V. L. J. Joly, P. A. Joy, M. W. Haverkort, H. Wu, A. Tanaka, H.-J. Lin, C. T. Chen, and L. H. Tjeng, Phys. Rev. B 77, 125124 (2008).

94. M. Nagel, I. Biswas, P. Nagel, E. Pellegrin, S. Schuppler, H. Peisert, and T. Chasse, Phys.Rev. B 75, 195426 (2007).

95. J. A. Mundy, Y. Hikita, T. Hidaka, T. Yajima, T. Higuchi, H. Y. Hwang, D. A. Muller, L. F. Kourkoutis, Nat Commun, **5**, 3464 (2014).

96. V. Leca, D. H. A. Blank, and G. Rijnders, arXiv:1202.2256 (2012).

97. R. Pentcheva and W. E. Pickett, Phys. Rev. Lett. 102, 107602 (2009).

98. A. Janotti, L. Bjaalie, L. Gordon, C.G. Van de Walle, Phys. Rev. B, 86, 241108 (2012).

99. N.C. Bristowe, P.B. Littlewood, E. Artacho, Phys. Rev. B, **83**, 205405 (2011).

100. L. Yu and A. Zunger, Nat. Commun. 5, 5118 (2014).

101. C. Cen, S. Thiel, G. Hammerl, C.W. Schneider, K.E. Andersen, C.S. Hellberg, J. Mannhart, J. Levy, Nat. Mater., 7, 298 (2008).

102. R. Colby, L. Qiao, K. H. L. Zhang, V. Shutthanandan, J. Ciston, B. Kabius, and S. A. Chambers, Phys. Rev. B 88, 155325 (2013).

103. J. M. D. Coey, M. Viret, S. von Molnár, *Adv. Phys.* **48**, 167 (1999).

104. C. Weber, K. Haule, G. Kotliar, Nat. Phys., **6**, 574 (2010).

105. P. Raychaudhuri, C. Mitra, P.D.A. Mann, S. Wirth, J. Appl. Phys. **93**, 8328 (2003).

106. Q. Zhang, W. Zhang, Phys. Rev. B **68**, 134449 (2003).

107. W. J. Lu, Y. P. Sun, B. C. Zhao, X. B. Zhu, W. H. Song, Phys. Rev. B **73**, 174425 (2006).

108. S. Middey, M. Kareev, D. Meyers, X. Liu, Y. Cao, S. Tripathi, D. Yazici, M. B. Maple, P. J. Ryan, J. W. Freeland, J. Chakhalian, Appl. Phys. Lett. **104**, 202409 (2014).

109. A. Gupta, T.R. McGuire, P.R. Duncombe, M. Rupp, J.Z. Sun, W.J. Gallagher, G. Xiao, Appl. Phys. Lett., **67**, 3494 (1995).

110. J. Töpfer, J.B. Goodenough, J. Solid State Chem., **130**, 117 (1997).

111. C. Aruta, M. Angeloni, G. Balestrino, N. G. Boggio, P. G. Medaglia, A. Tebano, B. Davidson, M. Baldini, D. Di Castro, P. Postorino, P. Dore, A. Sidorenko, G. Allodi, and R. De Renzi, J. Appl. Phys. 100, 023910 (2006).

112. Bovo, Laura & Moya, X & Prabhakaran, D & Soh, Yeong-Ah & Boothroyd, Andrew & Mathur, N.D. & Aeppli, G & Bramwell, S.T.. (2014). Restoration of the third law in spin ice thin films. Nature communications. 5. 3439. 10.1038/ncomms4439.

113. Hwang, HY. (2004). Ohtomo, A. & Hwang, H.Y. A high-mobility electron gas at the LaAl03/SrTiO3 heterointerface. Nature 427, 423-426. Nature. 427. 423-6. 10.1038/nature02308

Appendices

Appendix 1

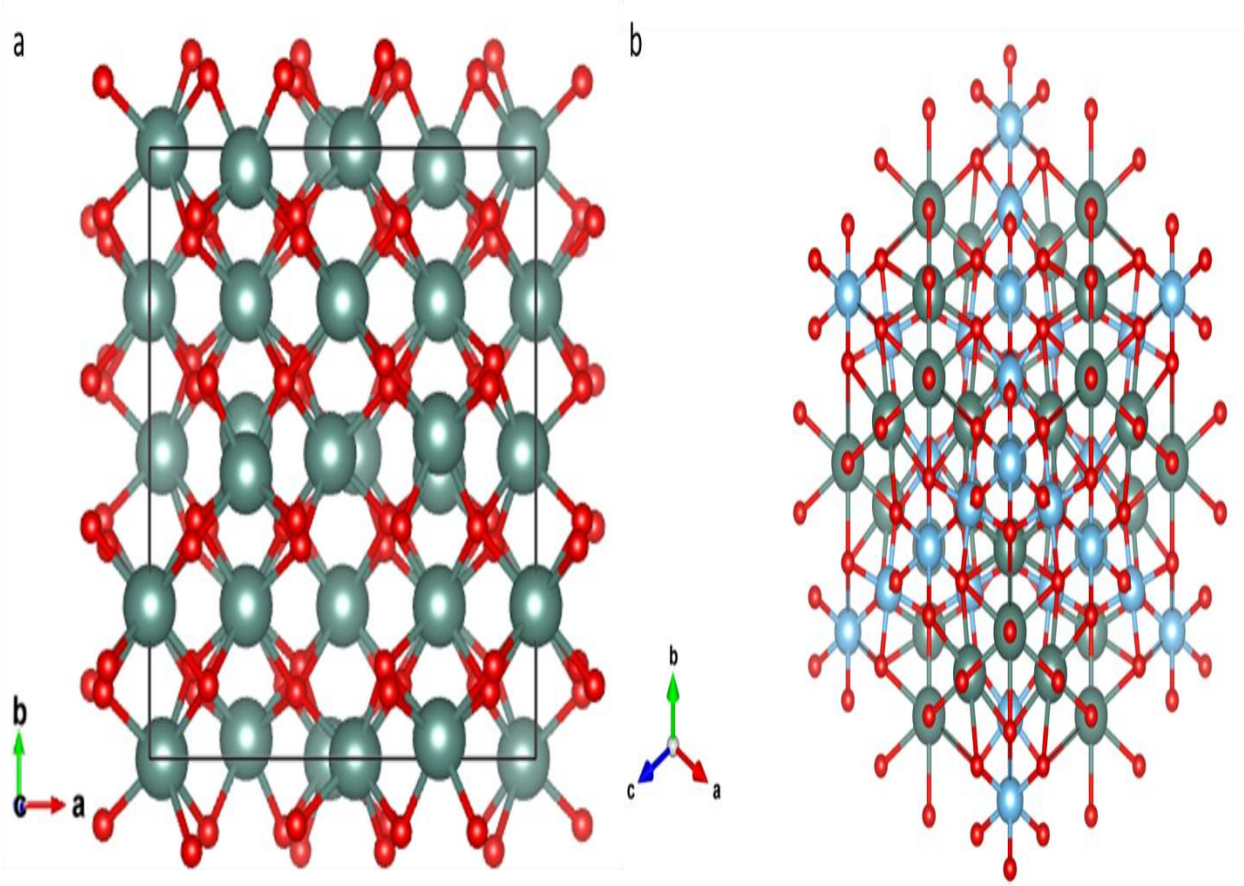

Figure 1.1 (a) is the YTO unit cell structure oriented along the (001) direction. (b) is the YTO unit cell oriented along the (111) and is our desired phase for growth

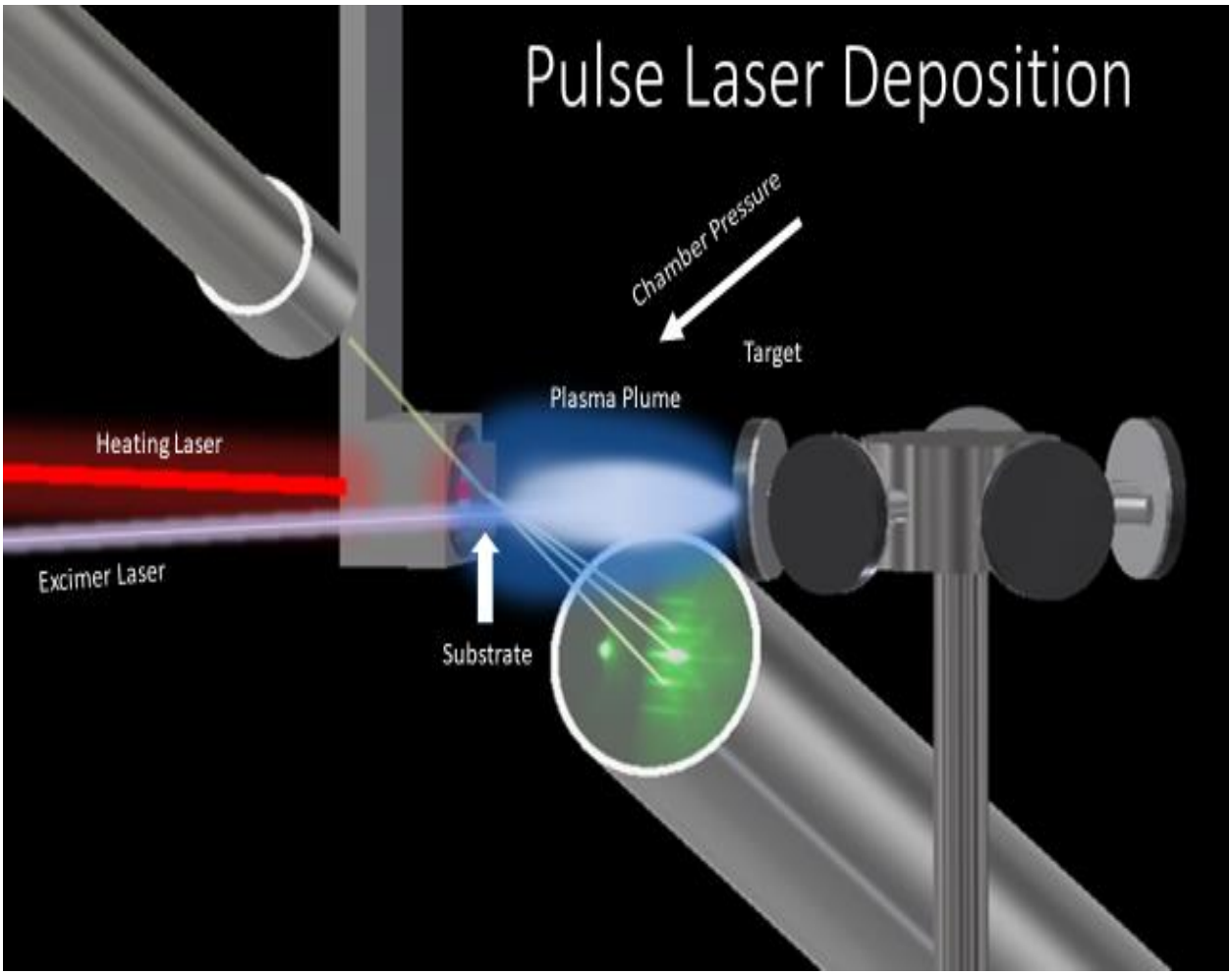

Figure 2.1 this is a schematic illustration of what the inside of a PLD chamber looks like during the deposition process with all of the different components being represented.

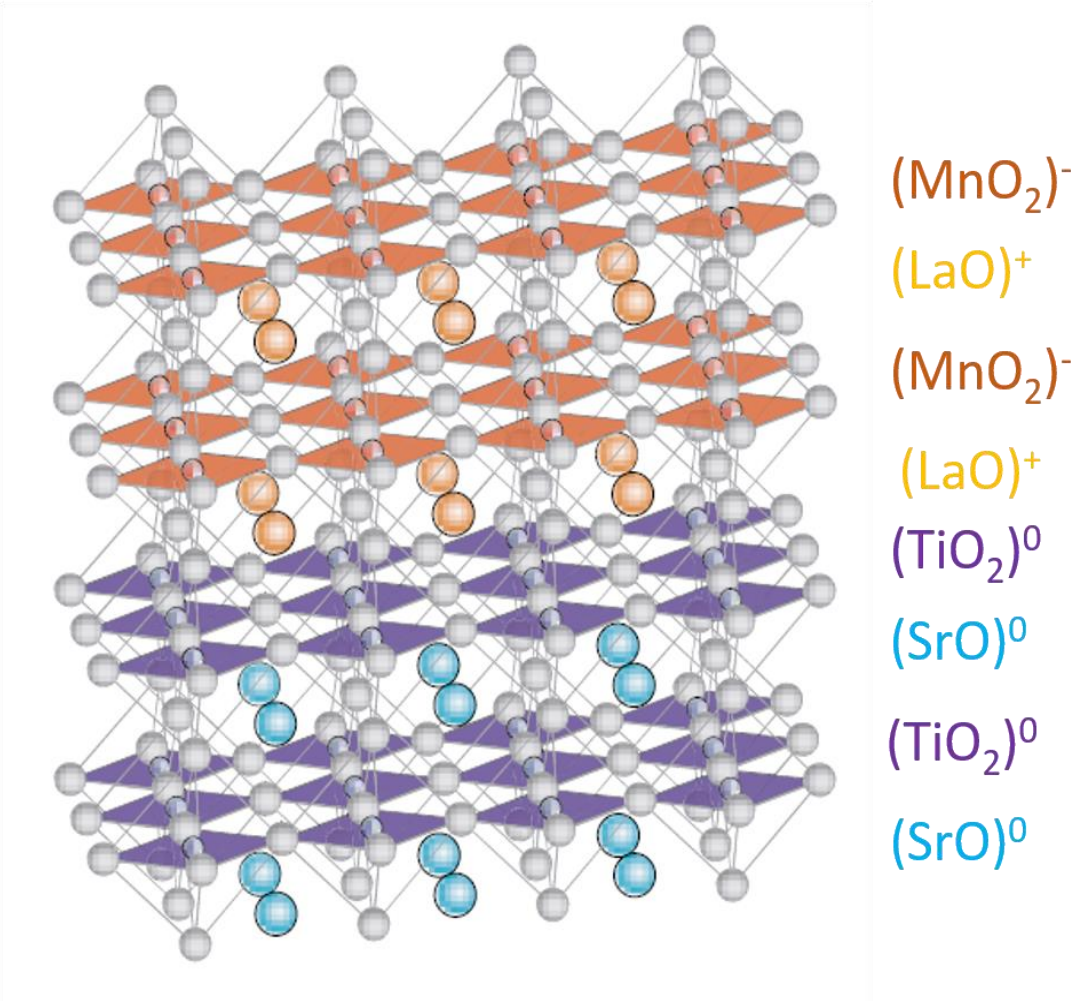

Figure 3.1 Illustration of the alternating layers of LMO on STO and the total charge of the each layer. [113]

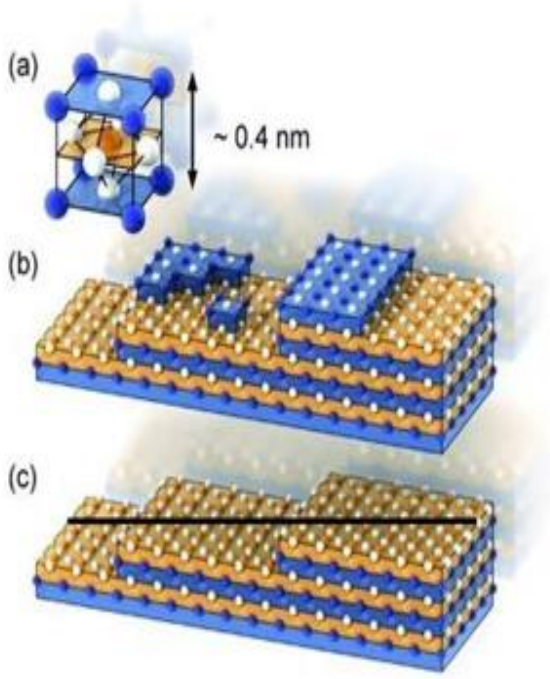

Figure 3.2 (a) is an illustration of a mixed unit cell of STO. (b.) this illustrates the initial mixed terminated state of the substrate before treatment; (c.) illustrates the singly terminated substrate surface after treatment.

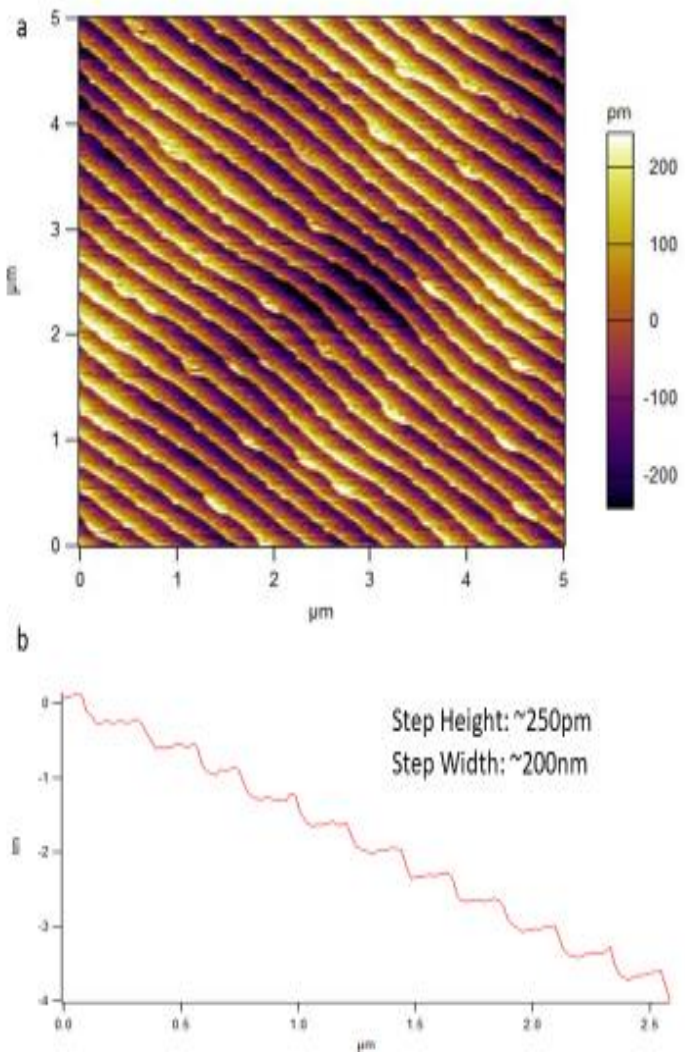

Figure 3.3 (a) AFM image of an STO substrate annealed at 1050°C in air for 2 hrs. (b) Step width (~200nm) and Height (250pm) trace showing single termination.

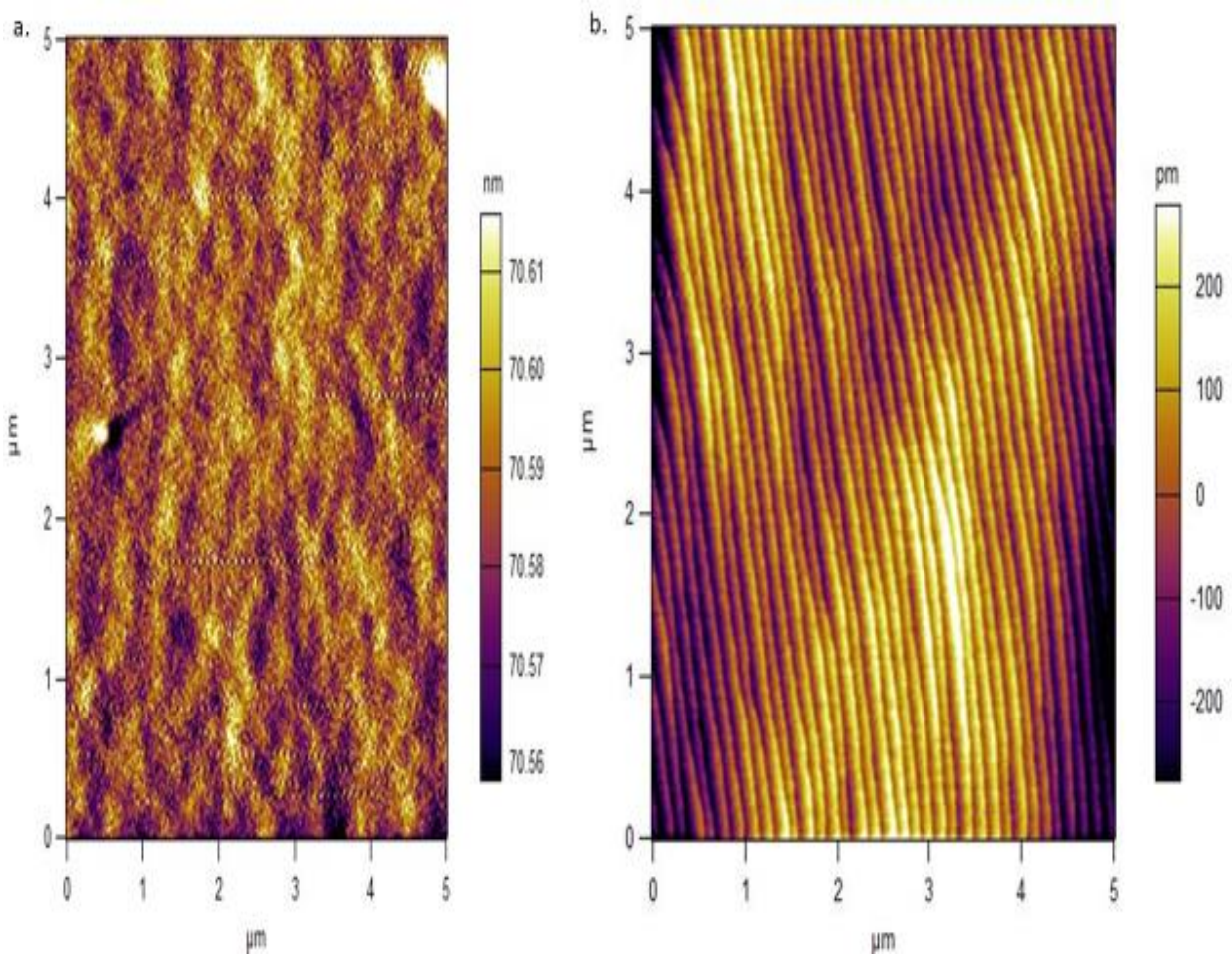

Figure 3.4 (a.) is an image of an NGO substrate as received; (b.) is an NGO substrate annealed for 3 hours at 1100°C in air. The singly terminated terraces can be seen.

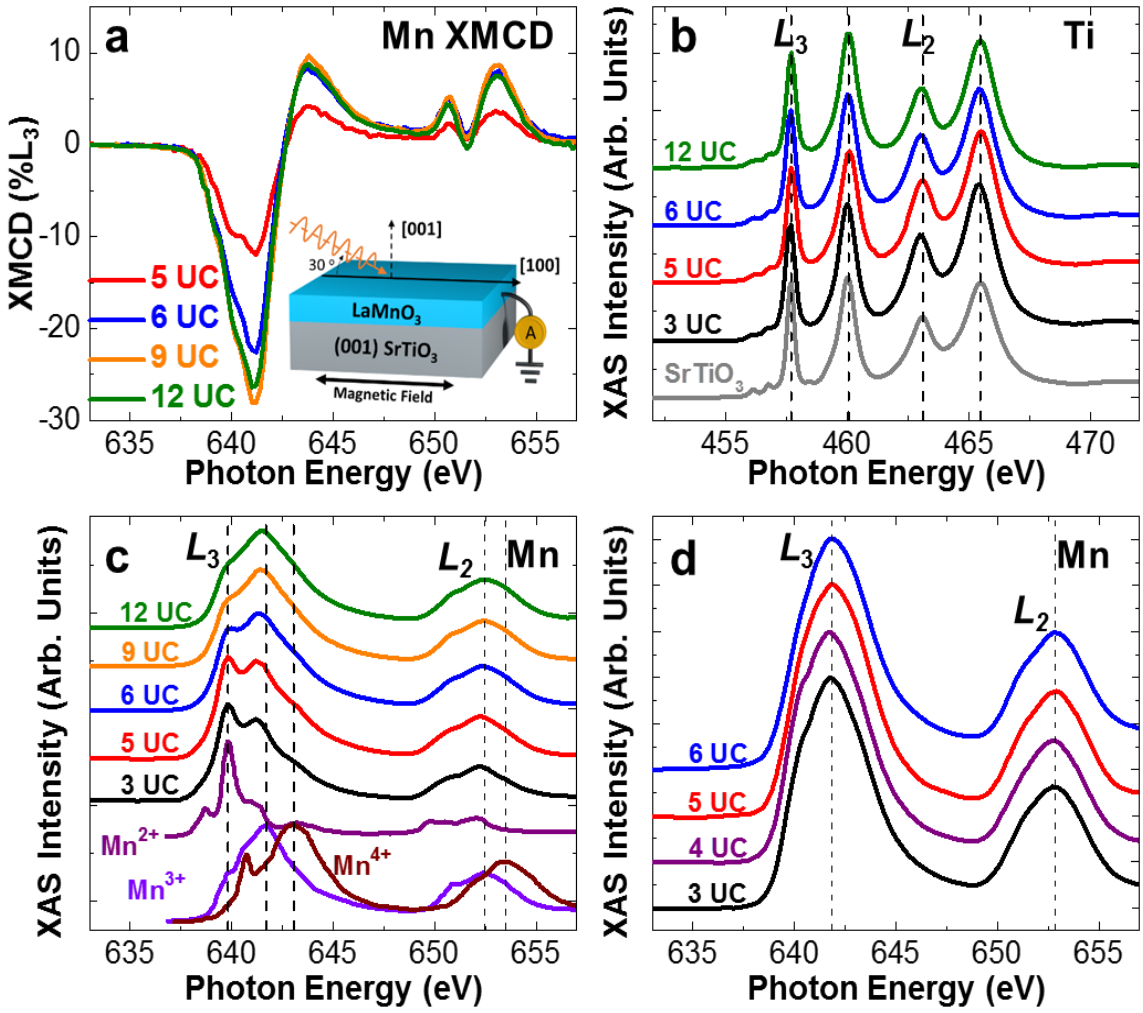

Figure. 3.5 (a) Mn XMCD spectra for various $LaMnO_3/SrTiO_3$ heterostructures. The inset shows a schematic of the experimental configurations for the X-ray spectroscopy studies. Thickness dependence of the XAS spectra of the $LaMnO_3/SrTiO_3$ heterostructures at the (b) Ti $L_{2,3}$, and (c) Mn $L_{2,3}$ edges with reference spectra for $SrTiO_3$, bulk $SrMnO_3$, $LaMnO_3$, and MnO for comparison. (d) XAS of Mn $L_{2,3}$ edges for various $LaMnO_3/NdGaO_3$ heterostructures where no reconstruction has occurred.

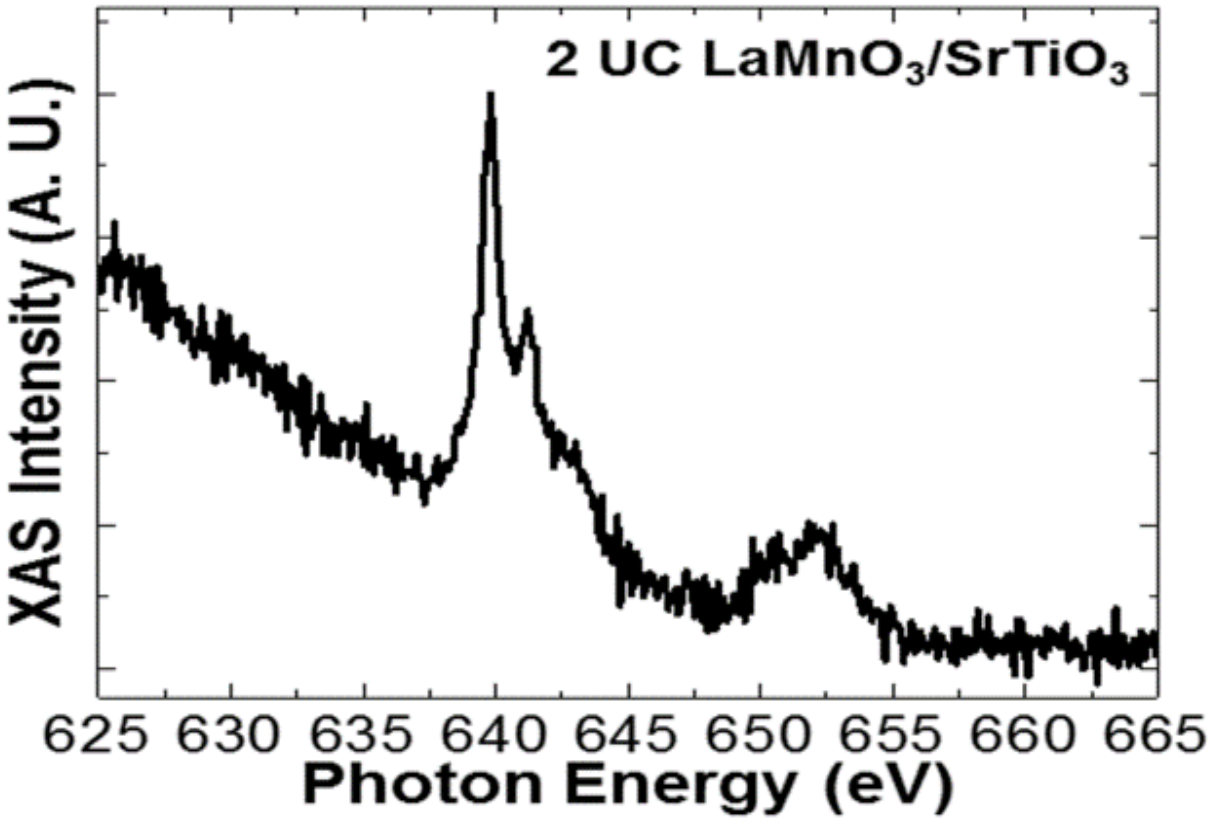

Figure 3.6 XAS spectrum about the Mn $L_{2,3}$ edges for a 2 unit-cell-thick $LaMnO_3/SrTiO_3$ heterostructure.

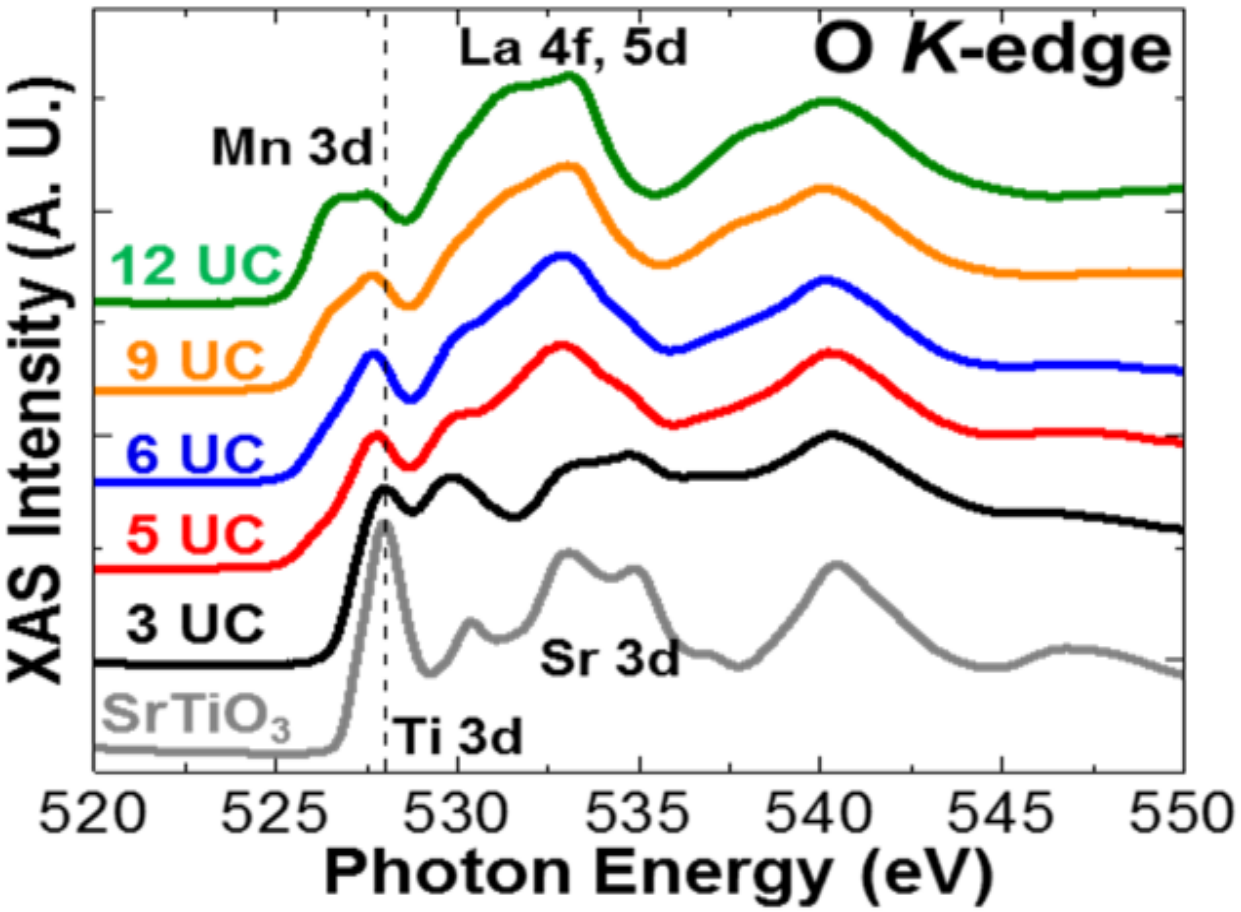

Figure 3.7 Thickness dependence of the XAS spectra of the O *K* edge of $LaMnO_3/SrTiO_3$ heterostructures with that for a bare $SrTiO_3$ substrate provided for comparison.

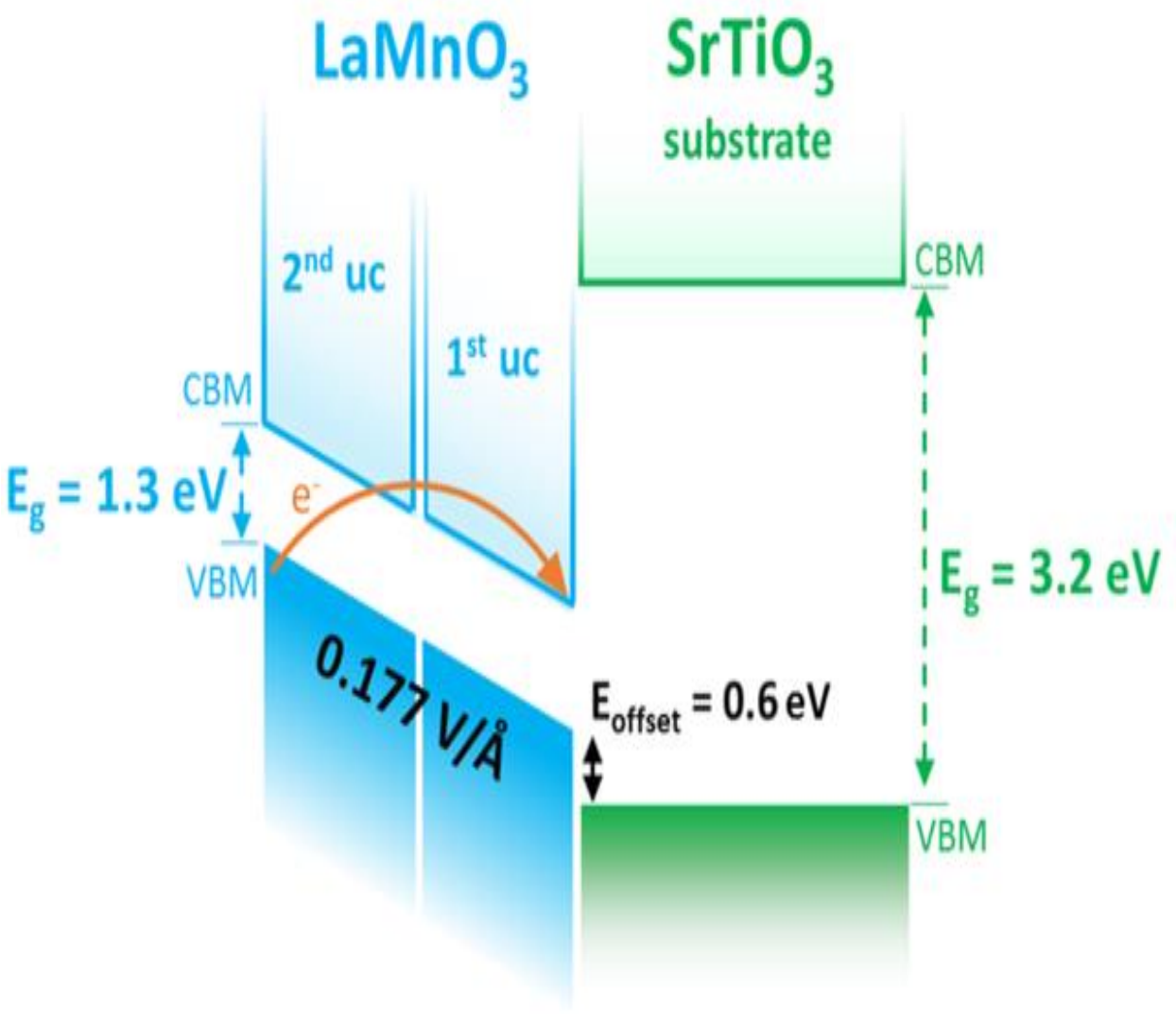

Figure 3.8 Schematic band diagram of $LaMnO_3/SrTiO_3$ interface. The electron moving from the top layer of the LMO sample to the bottom layer of the LMO sample is demonstrated by the orange curve.

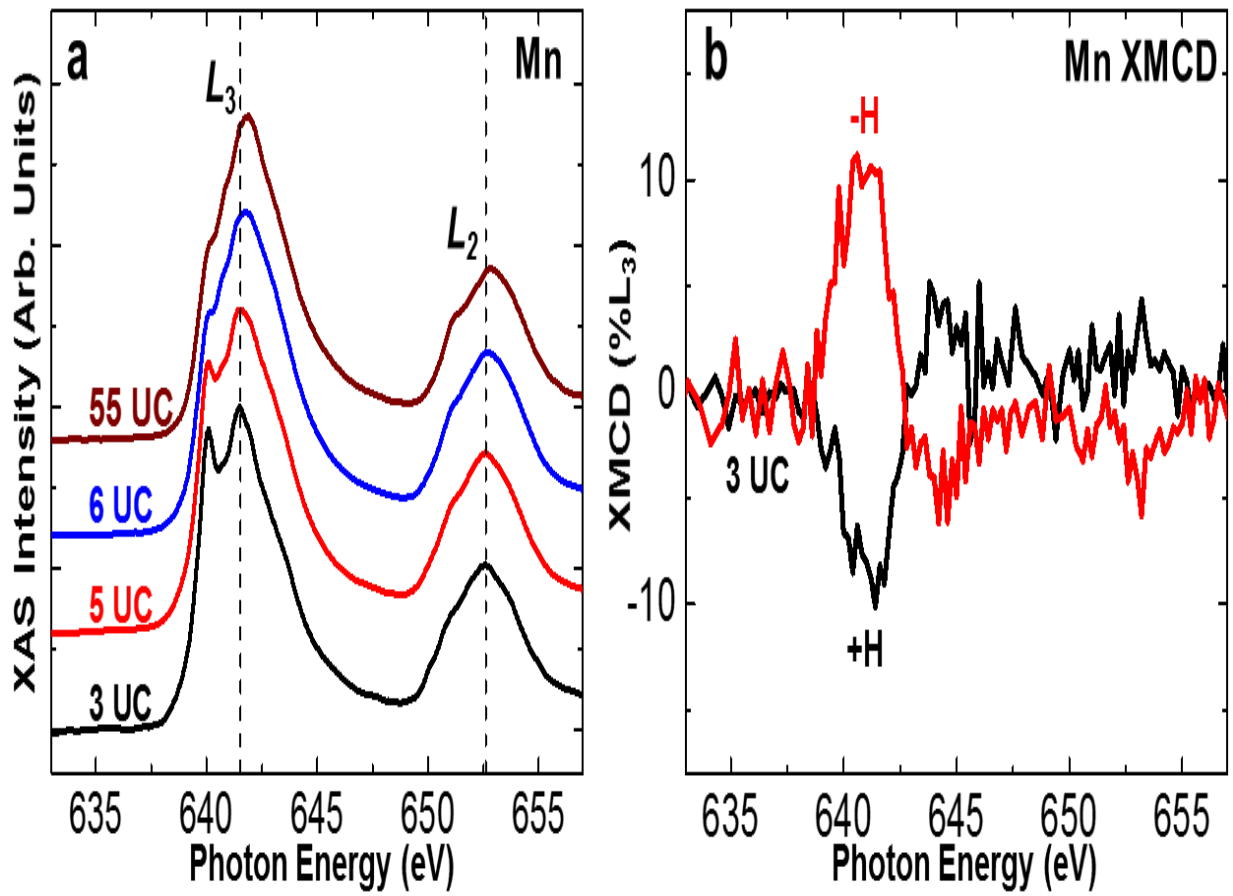

Figure 3.9 (a) Mn $L_{2,3}$ XAS spectra of the $La_{0.95}MnO_3/SrTiO_3$ heterostructures. (b) Mn XMCD spectra for the 3 UC $La_{0.95}MnO_3/SrTiO_3$ heterostructure. The XMCD features reverse in sign when the magnetic field is reversed, confirming the reliability of the observation.

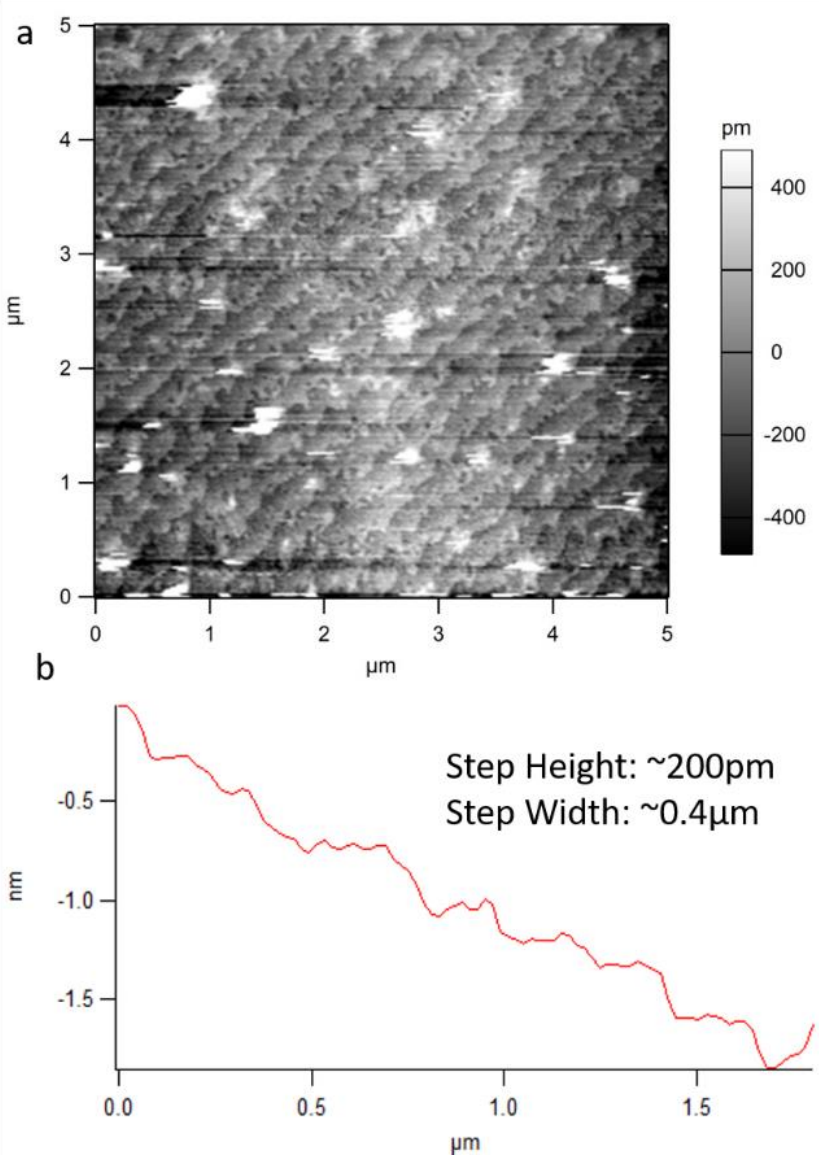

Figure 4.1 (a) AFM image of a YSZ substrate annealed in air at 1050°C for 2 hours. (b) Step (~0.4µm) and Height (200pm) trace showing single termination.

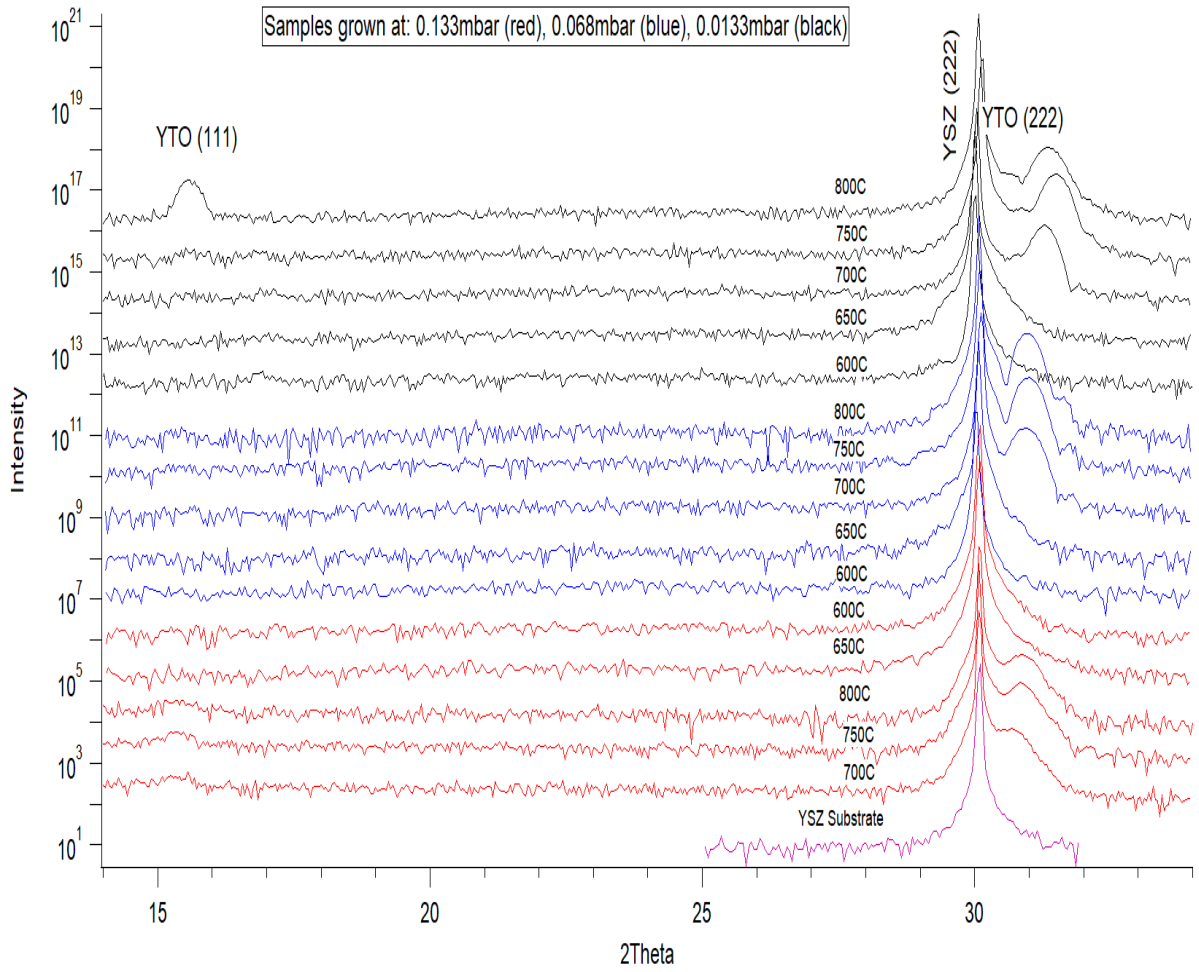

Figure 4.2 Plot of all samples grown. Peaks are prominent at 15.52°, 30°, and 31°.

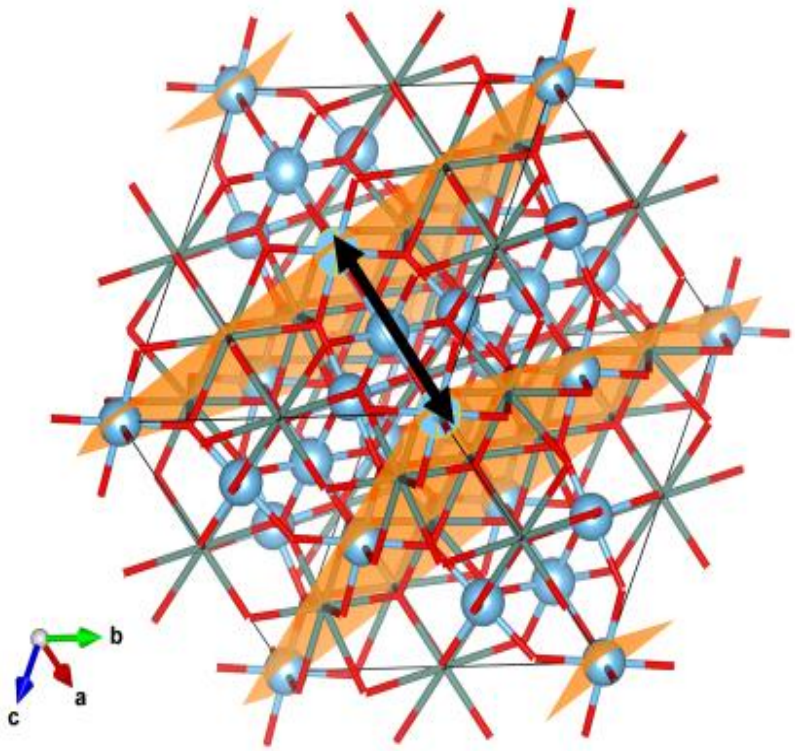

Figure 4.3 Image of a YTO crystal with planes along the (111) layers. Where the arrow illustrates the d spacing between the (111) layers.

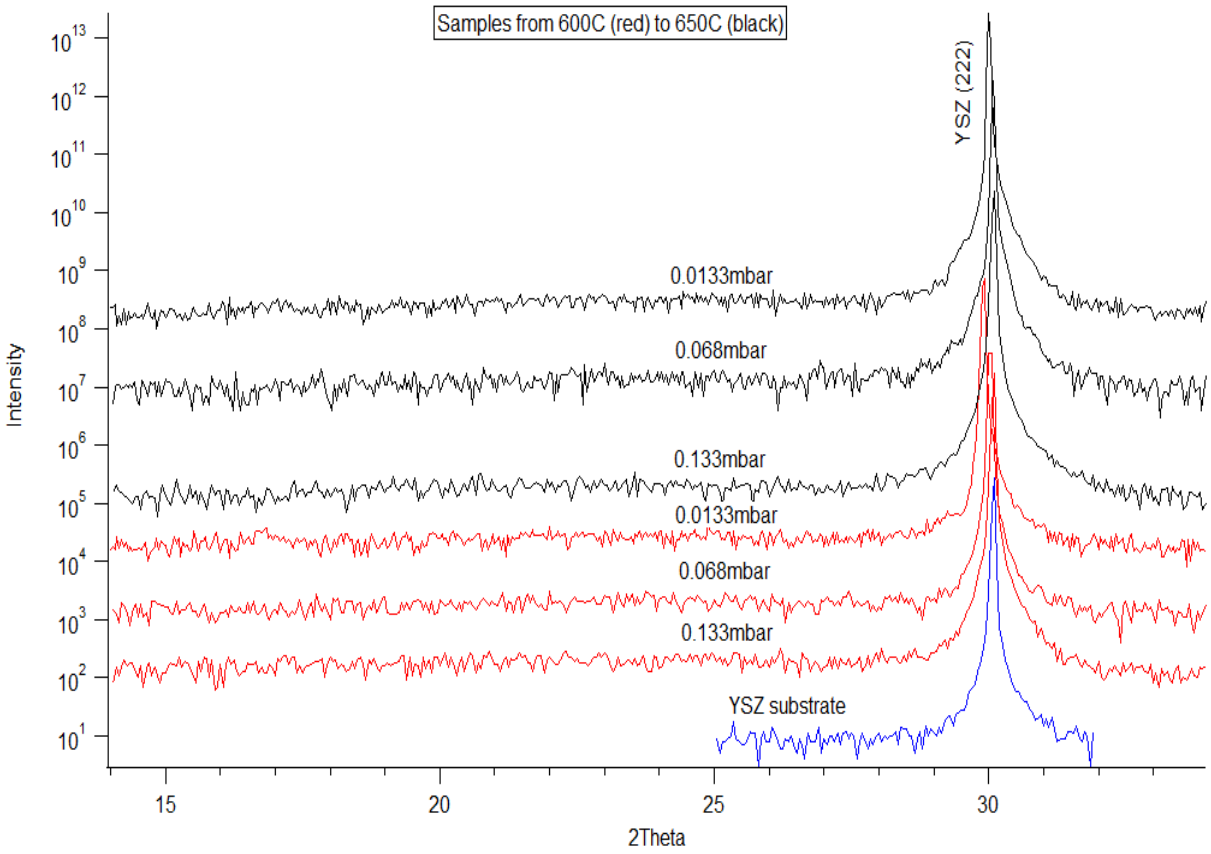

Figure 4.4 Plot of all samples grown from 600°C to 650°C. Only the substrate peak is detected.

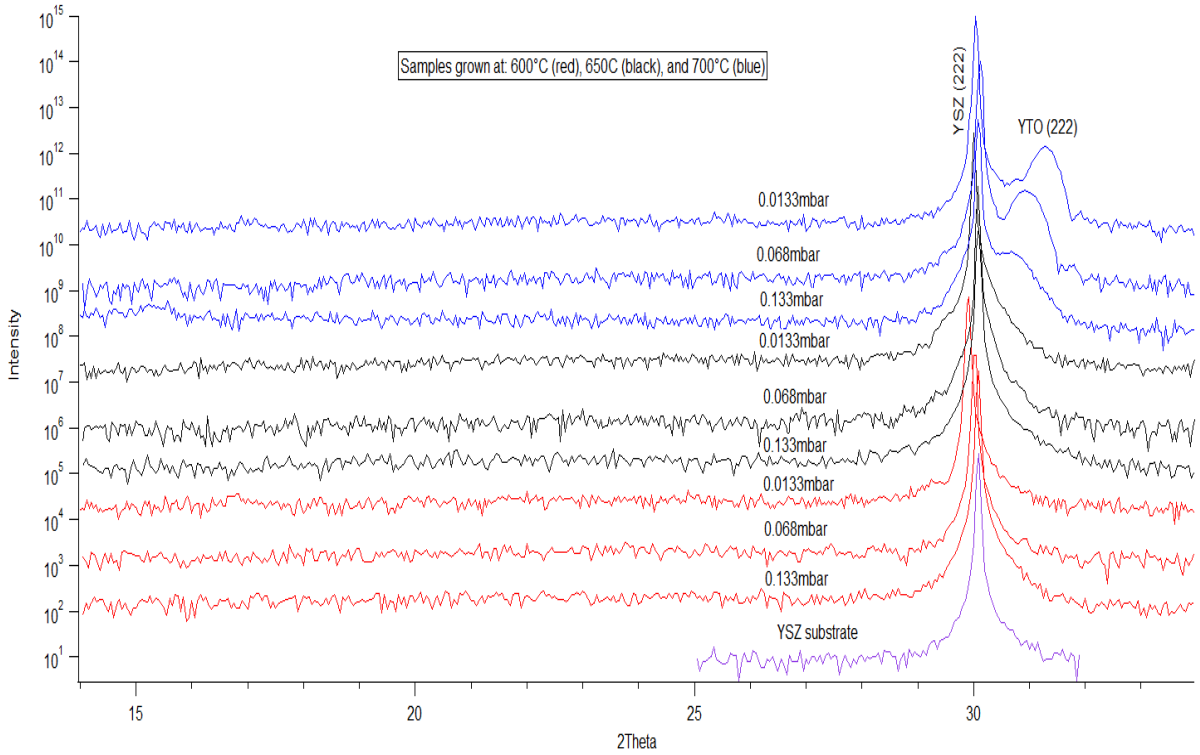

Figure 4.5 Plot of all of the samples grown at 600° C to 700°C. It is clear that there is no YTO (222) phase, or Y_2O_3 is absent for the 600° C to 650° C samples, but development of the peak at 31° is apparent for the samples grown at 700°C.

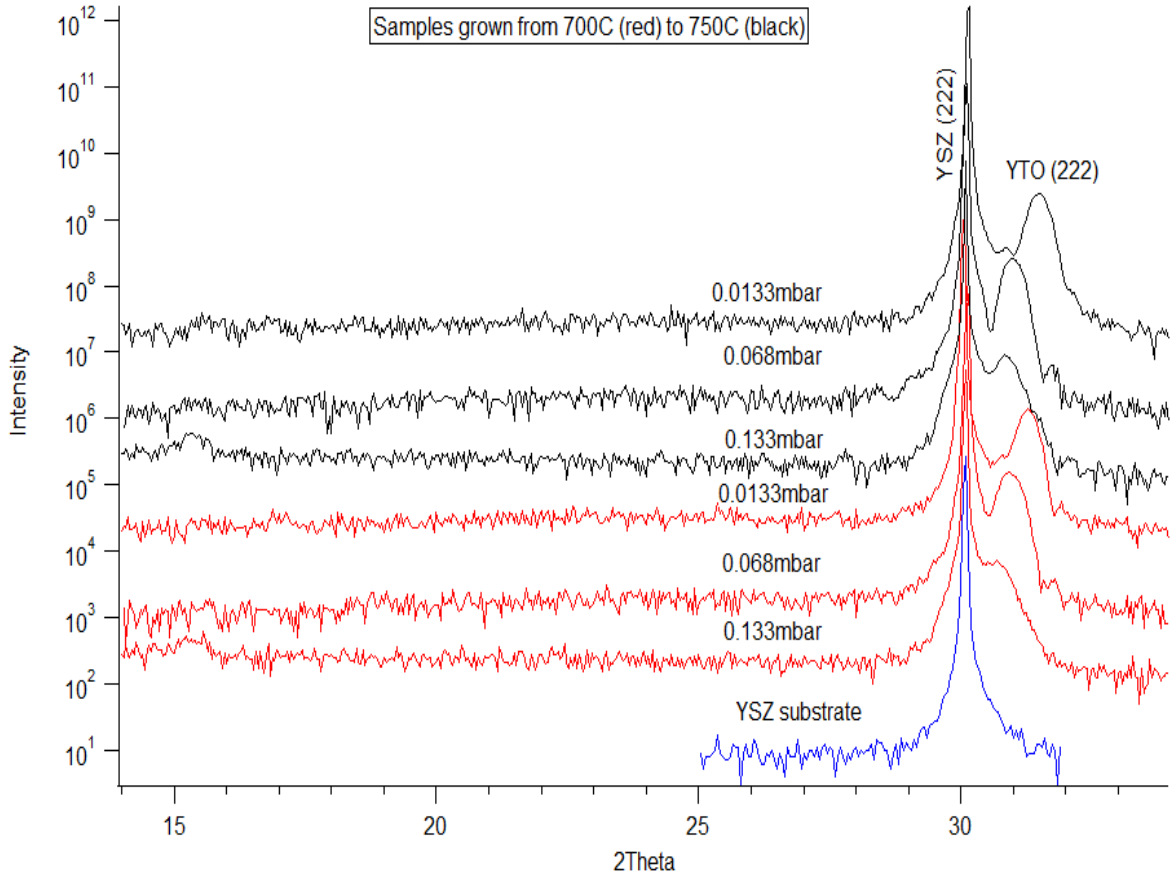

Figure 4.6 Plot of all of the samples grown at 700° C to 750°C. The peak appearing at the 31° is evidence for growth of either a YTO (222) phase, or Y_2O_3.

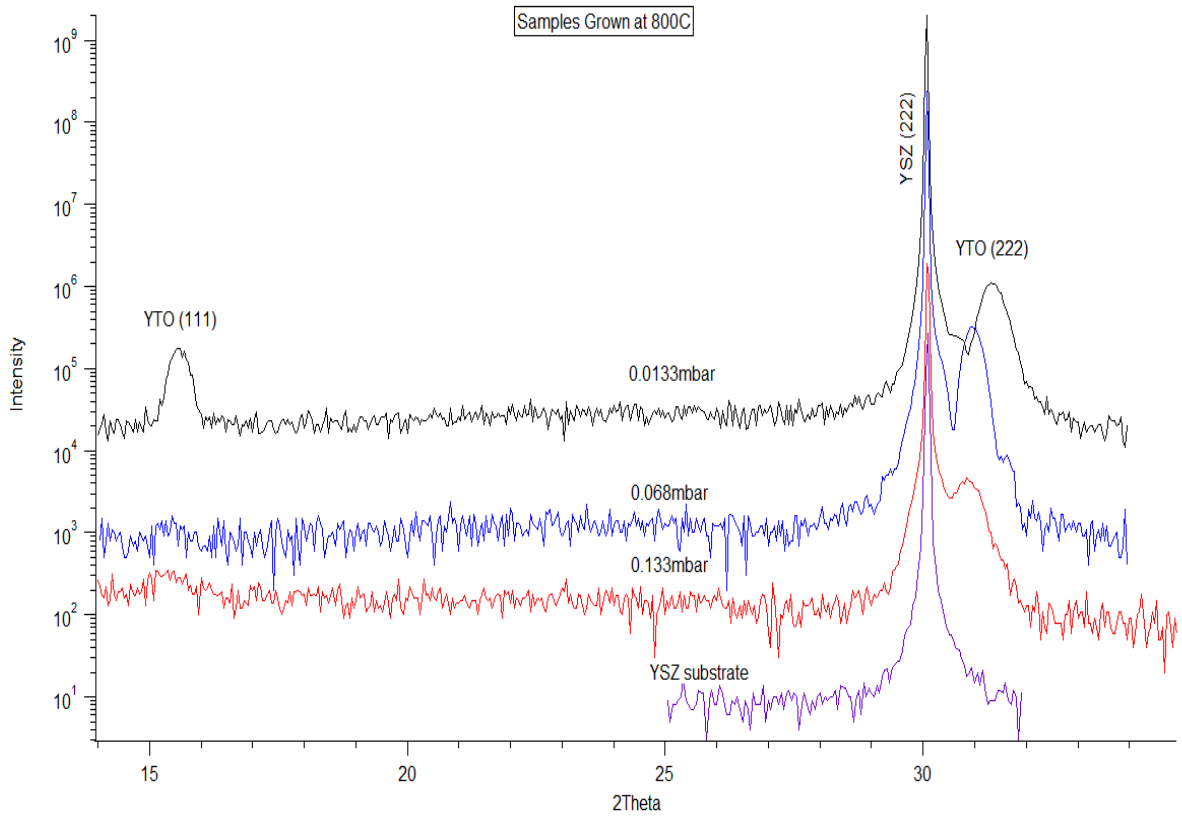

Figure 4.7 Graph of all samples grown at 800° C. Growth of the desired YTO (111) phase is indicated by the peak at 15.52°.

Appendix 2

Table 3.1 Treatment Conditions

Substrate	STO	NGO	YSZ
Treatment	BOE & DI water for 1 min each	Cleaned only	Cleaned only
Gas	Air	Air	Air
Temperature (°C)	1050°C	1100°C	1050°C
Time (Hrs)	2	3	2

Table 4.1 Growth Parameters

Sample	1	2	3	4	5	6	7	8	9	10	11	12	13	14	15
Preablation (2Hz)	1000	2000	1000	1000	500	500	500	500	500	500	500	500	500	500	500
Pressure (mbar)	0.13	0.13	0.13	0.13	0.13	0.068	0.068	0.068	0.068	0.068	0.0133	0.0133	0.0133	0.0133	0.0133
Valve Position	250	250	250	250	250	250	250	250	250	250	300	300	300	300	300
Flow Rate	250	20	20	20	20	20	20	20	20	20	1.3	1.3	1.3	1.3	1.3
Temperature(°C)	700	750	800	651	602	602	651	702	752	801	601	651	701	751	801
Laser Energy (mJ)	300	304	294	332	328	330	328	327	353	353	350	351	364	366	355
Laser Pressure (mbar)	3420	3451	3452	3396	3422	3461	3469	3470	3412	3451	3440	3456	3424	3454	3458
Laser Voltage (kV)	18.3	18.3	18.3	19.5	19.5	19.5	19.5	19.5	18.1	18.1	18.1	181	18.3	18.3	18.3
Heater Power (W)	18	23	27	12	12	11	15	17	20	24	12	14	17	21	24
Heater Current (A)	5	6	6.7	4	4.1	4	4.5	5	5.5	6.3	4.2	4.4	4.8	5.5	6.2
Number of Pulses (2Hz)	2000	2000	2000	2000	2000	2000	2000	2000	2000	2000	2000	2000	2000	2000	2000
Attenuator used	No	No	No	No	No	No	No	No	Yes (2)	Yes (2)	Yes (2)	Yes (2)	Yes (2)	Yes (2)	Yes (2)
Large Mask used	Yes	Yes	Yes	Yes	Yes	Yes	Yes	Yes	Yes	Yes	Yes	Yes	Yes	Yes	Yes

Vita

Clayton Frederick was born in Gadsden, Al and is the youngest of three children. After working for a few years as a correctional officer for the State of Alabama Department of Corrections, he started phlebotomy while attending Gadsden State Community College. He subsequently transferred to The Alabama A & M University in Huntsville, Al for his Bachelors of Science in physics graduating Magna Cum Laude in December 2014. In the fall of 2015, he accepted a graduate teaching assistantship at the University of Tennessee, Knoxville, in the department of Physics and Astronomy, while pursuing his graduate studies. That fall semester in 2015 he conducted research in condensed matter physics, and continued working in the materials science field until graduating with a Master's of Science degree in Physics in August 2018.